A Synoptic Climatological Analysis of the Atmospheric Drivers of Water Clarity Variability in the Great Lakes

ERIK T. SMITH,[a] CAMERON C. LEE,[a] BRIAN B. BARNES,[b] RYAN E. ADAMS,[a] DOUGLAS E. PIRHALLA,[c] VARIS RANSIBRAHMANAKUL,[c] CHUANMIN HU,[b] AND SCOTT C. SHERIDAN[a]

[a] *Department of Geography, Kent State University, Kent, Ohio*
[b] *College of Marine Science, University of South Florida, Saint Petersburg, Florida*
[c] *National Oceanic and Atmospheric Administration/National Center for Coastal Ocean Science, Silver Spring, Maryland*

(Manuscript received 20 June 2019, in final form 2 January 2020)

ABSTRACT

A historical water clarity index (K_d index or KDI) was developed through the use of satellite-derived and validated diffuse light attenuation (K_d; m^{-1}) for each of the Great Lakes (and subbasins) on a daily level from 1998 to 2015. A statistical regionalization was performed with monthly level KDI using *k*-means clustering to subdivide the Great Lakes into regions with similar temporal variability in water clarity. The KDI was then used to assess the relationship between water clarity and atmospheric circulation patterns and stream discharge. An artificial neural-network-based self-organized map data reduction technique was used to classify atmospheric patterns using four atmospheric variables: mean sea level pressure, 500-hPa geopotential heights, zonal and meridional components of the wind at 10 m, and 850-hPa temperature. Stream discharge was found to have the strongest relationship with KDI, suggesting that sediments and dissolved matter from land runoffs are the key factors linking the atmosphere to water clarity in the Great Lakes. Although generally lower in magnitude than stream discharge, atmospheric circulation patterns associated with increased precipitation tended to have stronger positive correlations with KDI. With no long-range forecasts of stream discharge, the strong relationship between atmospheric circulation patterns and stream discharge may provide an avenue to more accurately model water clarity on a subseasonal-to-seasonal time scale.

1. Introduction

The Great Lakes Basin is an ecologically diverse region, home to more than 3500 plant and animal species, nearly 34 million people, and 84% of North America's freshwater (Fuller et al. 1995). More than 30% of the U.S. and Canada's gross domestic product is generated in the region (Krantzberg and Boer 2006). In recent decades, water clarity across most of the Great Lakes has increased, a trend observed both through field observation and through the interpretation of data from various remotely sensed observations (Binding et al. 2007; Fig. 1). This trend is thought to be associated with the increase in invasive mussel species in recent decades, contributing to reductions in phytoplankton biomass and disruptions in food chain dynamics (Binding et al. 2007; Vanderploeg et al. 2001; Rennie et al. 2009; Nalepa et al. 2009). The mussels increase water clarity by removing particulate matter at a rate of up to one liter per mussel per day (Binding et al. 2007; Nalepa et al. 2010; Ransibrahmanakul et al. 2018; Shuchman et al. 2017) and stimulate benthic plant growth by enhancing the amount of light penetration in the water (Ricciardi et al. 1997; Skubinna et al. 1995). In other areas, particularly western Lake Erie, water clarity has decreased as a result of cyanobacterial blooms and resuspension of inorganic matter (Millie et al. 2009; Makarewicz et al. 1999; Binding et al. 2007). These cyanobacterial blooms are exacerbated by the influx of high concentrations of nutrients through eutrophication (Scavia et al. 2014). The increase in nutrients, particularly phosphorus, into the western basin of Lake Erie is primarily related to regional agricultural practices, with increased eutrophication following large precipitation events during spring (Michalak et al. 2013; Watson et al. 2016). Collectively, these water clarity changes have profound ecological impacts. While many of the changes in the Great Lakes can be traced

Corresponding author: Erik T. Smith, esmit149@kent.edu

DOI: 10.1175/JAMC-D-19-0156.1

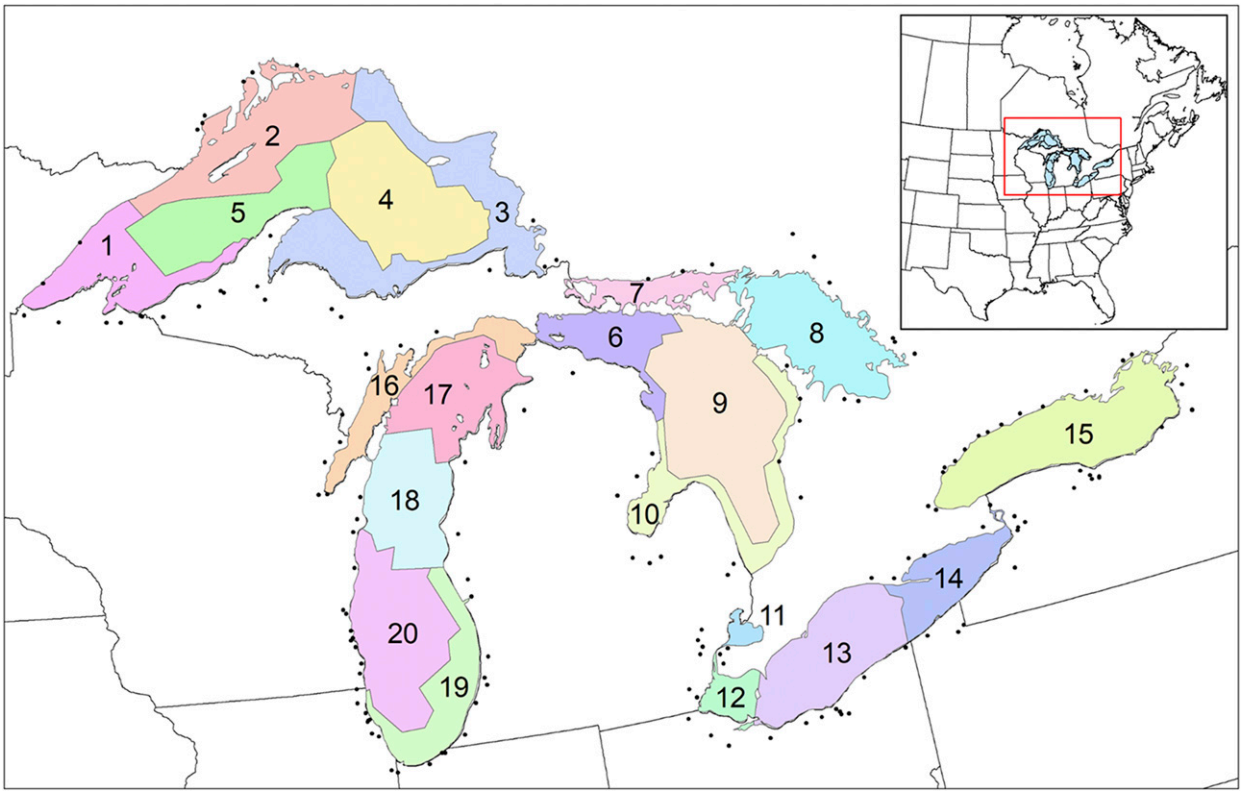

FIG. 1. Final regions and gauging stations. The inset map shows the spatial extent of the 500z SOM, with the red outline showing the spatial extent of the 850t and UVwind SOMs. The spatial extent of the MSLP SOM is similar to that of the 500z SOM (inset) but is 5° smaller in each direction.

to anthropogenic influences such as the introduction of invasive species as well as industrial and agricultural pollution, anthropogenic forcing and climate change should also be considered primary contributors to changes in water clarity over time (Shuchman et al. 2017).

In contrast to many other water basins, both turbid and excessively clear water may trigger negative environmental responses. Lakes Michigan and Huron have experienced a decrease in chlorophyll-a concentration as water clarity has increased (Barbiero et al. 2011; Fahnenstiel et al. 2010), leading to a significant reduction in food supply for many of the crustacean species (Barbiero et al. 2011). Meanwhile, the decrease in water clarity in western Lake Erie has resulted in an increase in toxic cyanobacteria (Michalak et al. 2013). Understanding the role of climate on these complex ecosystem–stressor interactions is vital to developing a consistent water clarity index applicable for each basin.

Synoptic climatology has been used to identify atmospheric patterns and their relationship to long-term changes and variability in ocean chlorophyll levels (Sheridan et al. 2013), anomalously cold sea surface temperature events (Pirhalla et al. 2014), and overall water clarity (Sheridan et al. 2014), for coastal ocean waters of the southeastern United States. The Great Lakes system differs from ocean water in several aspects, including the presence of seasonal ice cover and seasonal variability in stream discharge, along with various other environmental stressors that affect this closed freshwater system. Water temperature has been shown to play an important role in the growth, survival, and distribution of many species (Dobiesz and Lester 2009; Trumpickas et al. 2009). Wind has also been shown to influence water clarity not only by increasing suspended particles but also indirectly by altering the lake temperature profile (Niemistö 2008; Thiery et al. 2014). Despite current evidence of the severity of the invasive mussel problem, knowledge is limited concerning how climate variability, weather systems, mussels (zebra and quagga), land use changes and other factors interact as coupled systems.

Traditionally, water clarity is measured as the Secchi disk depth (SDD; m), that is, the depth at which a black–white disk is no longer visible to a human eye (Lee et al. 2018). SDD is inversely proportional to the diffuse downwelling light attenuation coefficient (K_d; m^{-1}) at the wavelength where light penetrates the deepest

TABLE 1. The number of retained principal components and the explained variance of the retained PCs for each atmospheric variable.

Variable	Retained PCs	Explained variance
500z	26	99.37
MSLP	22	98.81
850t	4	98.69
UVwind	49	98.60

(Lee et al. 2018), usually in the blue or blue-green region of the visible light. The two major contributors to K_d are particles (including living particles such as phytoplankton and nonliving particles such as sediments, both contributing to water turbidity) and colored dissolved organic matter (Davies-Colley and Smith 2001), both of which are rich in stream discharge, particularly in a closed system like the Great Lakes. However, long-term forecasts of stream discharge are not available, preventing it from being used as a variable in forecasts of water clarity. This study develops a historical water clarity index [K_d index (KDI)] for the Great Lakes to assess the connection between water clarity, stream discharge, and atmospheric circulation patterns (CPs) to improve the ability to forecast extreme water clarity episodes in the Great Lakes on a seasonal time scale.

2. Data and methods

a. Water clarity data and geographic regionalization

Level 2 multispectral remote sensing reflectance (R_{rs}; sr^{-1}) data from the Moderate Resolution Imaging Spectroradiometer (MODIS/*Aqua*, with native spatial resolution at nadir of ~1 km) spanning the months July 2002–December 2015 (15 359 files) within the bounds from 1° to 49°N and from 76° to 92°W were downloaded from the National Aeronautics and Space Administration (NASA) Goddard Space Flight Center ocean color website (http://oceancolor.gsfc.nasa.gov). Each granule (i.e., file) was mapped to an equidistant rectangular projection with 1-km spatial resolution. Pixels with negative R_{rs} at any wavelength were excluded from

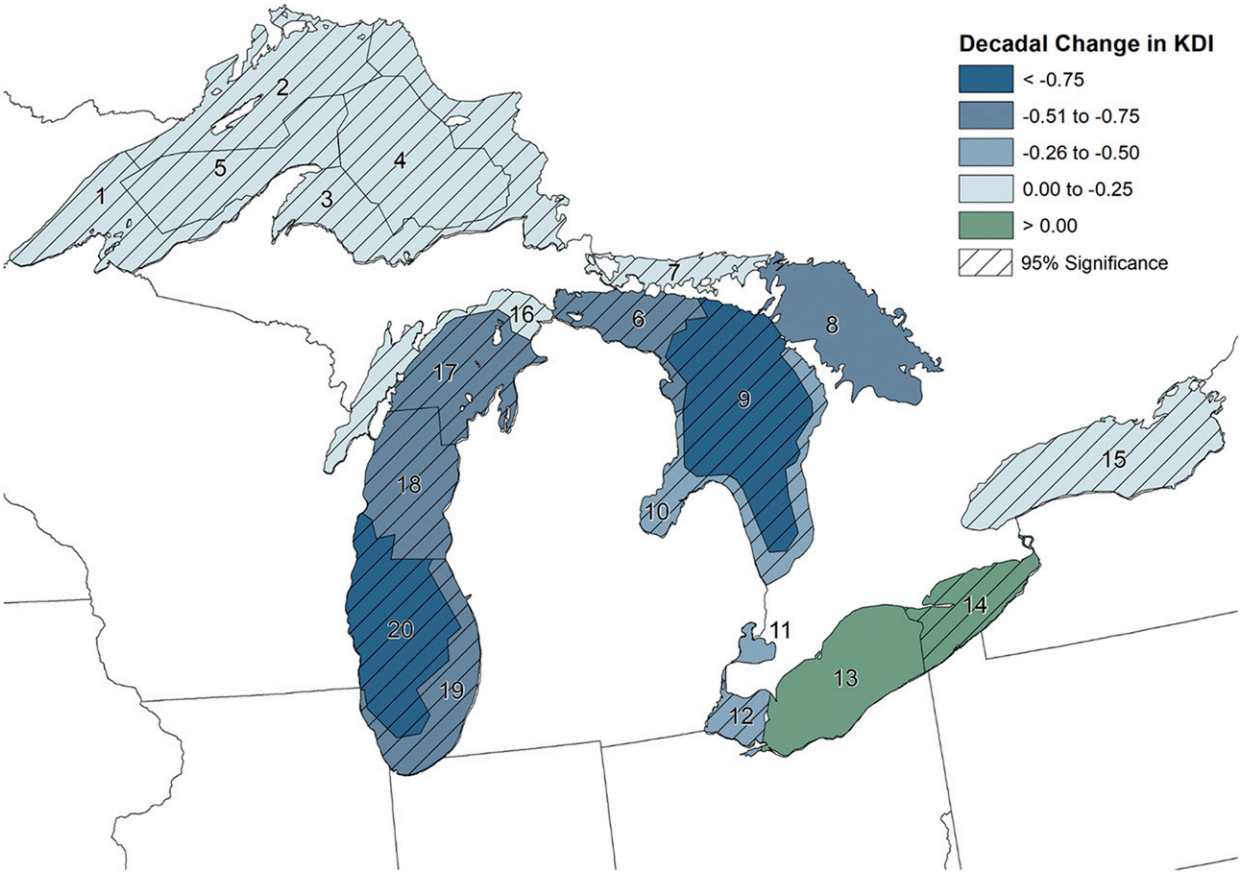

FIG. 2. Decadal change in KDI from 1997 to 2015. Significance at the 95% confidence level is denoted with hatching. Positive values indicate decreased water clarity; negative values indicate increased water clarity.

analysis, as were pixels identified by any of the NASA standard level 3 flag suite (see https://oceancolor.gsfc.nasa.gov/atbd/ocl2flags/). Reflectance data were used to calculate K_d at 488 nm [K_d(488)] via the Kd_lee algorithm (Lee et al. 2005) and were subsequently used for regionalization and time series analyses. The Kd_lee algorithm decomposes the spectral R_{rs} data to absorption and backscattering coefficients, from which K_d(488) was estimated. Validation using field-measured K_d showed that Kd_488_lee is more accurate than other satellite-based K_d data for productive waters [e.g., when $Kd(488)$ is $> 0.3\,m^{-1}$] (Zhao et al. 2013). Monthly mean Kd_488_lee data were calculated for each 1 km location in the Great Lakes region during each month. Monthly mean and standard deviation climatologies of Kd_488_lee were also calculated. For each month, the monthly mean Kd_488_lee data were then compared to these Kd_488_lee climatologies in order to calculate a KDI for each pixel, as

$$\text{KDI} = (\text{monthly\_mean} - \text{monthly\_mean\_climatology}/\text{monthly\_stdev\_climatology}). \quad (1)$$

To quantify spatially varying climate–KDI relationships, we undertook a statistical regionalization using a k-means clustering of monthly level KDI data to divide the Great Lakes into 20 regions. The clustering method and number of regions were selected by assessing multiple clustering algorithms [k-means, self-organized maps (SOMs), average linkage hierarchical, and Ward's linkage hierarchical] and multiple numbers of clusters (including SOMs from sizes 3×3 to 6×6 and from $k = 5$ to $k = 15$ for the other clustering algorithm options) with clustering validation metrics [the Calinski–Harabasz criterion, the Davies–Bouldin criterion, the silhouette criterion, the variability skill score (Lee 2014), and the distributed variability skill score (Lee 2017)]. Of nearly 50 different options, the best-performing clustering solution was k means with a 15-cluster solution. While most of the 15 regions were spatially homogenous, some were split into multiple lakes, necessitating the hand drawing of the final regions in ArcMap (using the clustering results as the framework). Regions that were clustered into the same regions but split geographically were simply identified as separate regions, ultimately resulting in an extra five regions added to the original 15-cluster solution derived from clustering and yielding the final 20-region map used in all further analyses (Fig. 1).

Spatially averaged KDI data for these 20 regions were then calculated with daily temporal resolution. Specifically, for each calendar date ($N = 366$), 30-day running climatological mean and standard deviation

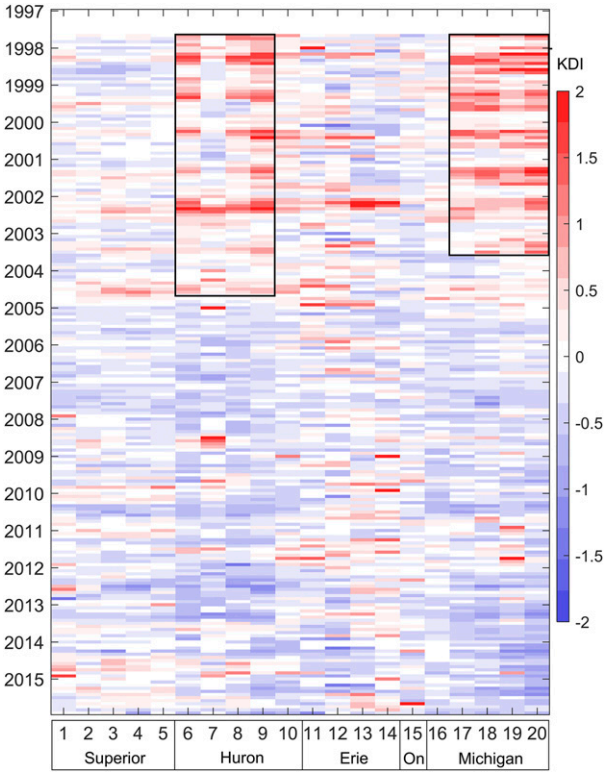

FIG. 3. KDI by month from 1997 to 2015 for each region (x axis). KDI is normalized for each region (columns), where red denotes low water clarity (high KDI) and blue denotes higher water clarity (lower KDI) relative to the region. The black-outlined boxes highlight a period of high KDI for Lake Huron (on the left) and Lake Michigan (on the right).

maps were developed. Pixel-specific daily mean Kd_lee data from each day in the MODIS time series were then compared to these climatological values to derive KDI in a manner similar to Eq. (1), except that daily mean values were compared to the corresponding running mean and standard deviation climatologies (i.e., those climatologies centered on the calendar date of the day of interest). Note, to account for the increased spatial heterogeneity in the daily mean data (relative to monthly means), a 5×5 median filter was applied to each individual MODIS image prior to daily mean calculation. From the KDI maps, daily mean KDI at each of the 20 regions was calculated for use in subsequent analysis of water clarity–climate relationships. Regional KDI values were retained for further analyses if at least 5% of the pixels in the region had data—a threshold determined based upon previous research using the KDI (Lee et al. 2017). Percentiles were calculated for each region's KDI distribution and used to examine trends in extreme clear KDI events (20th percentile) and turbid KDI events (80th percentile). The KDI was then linearly detrended to remove

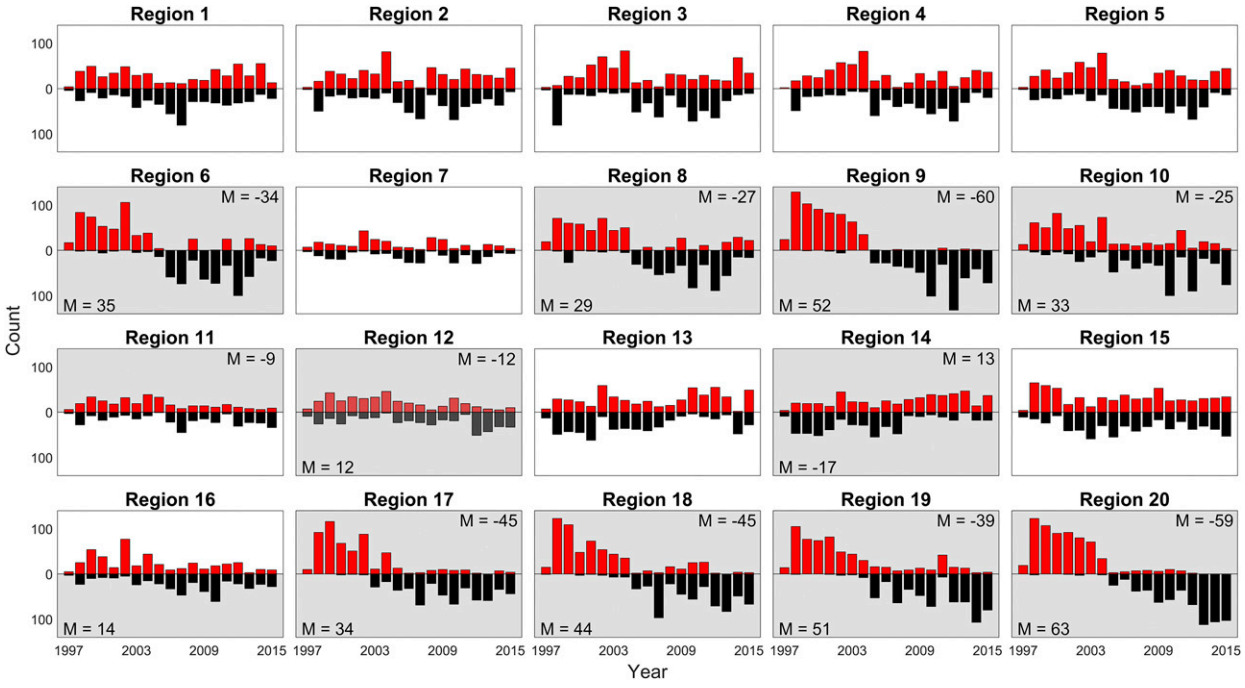

FIG. 4. Count of 20th-percentile (black—clearer water) and 80th-percentile (red—less clear water) KDI events by year. Regions with significant changes are highlighted with a gray background with the decadal slope *M* shown for both the 80th-percentile (in upper right of panel) and 20th-percentile (in bottom left of panel) events.

the trends related to regional changes in mussel population throughout the study period. This was particularly important in Lakes Michigan and Huron where a large increase in water clarity has been observed in recent decades.

b. Synoptic climatological analysis

Hydrological data were acquired to examine the relationship of water clarity with stream discharge and precipitation. The stream discharge ($m^3 s^{-1}$) data were gathered from reliable U.S. (U.S. Geological Survey 2017) and Canadian (Water Survey of Canada 2017) streamflow gauging stations near each lake. The gauging stations were divided according to the lake regions (Fig. 1) in which the stream ends. Regions 4 and 9 had no gauging stations with at least 25 years of data, therefore the nearest station from an adjacent region was used instead. A generalized linear model was used to determine the relationship between stream discharge volume and KDI. Daily precipitation totals across the region of study were acquired from the National Centers for Environmental Prediction North American Regional Reanalysis (NARR; Mesinger et al. 2006). The mean daily precipitation was determined for each region by using the NARR grid points over each lake's watershed, rather than over the lake itself, as the former method resulted in higher Pearson-based correlations between precipitation and water clarity than the latter.

For the synoptic climatological analysis, this study utilized four atmospheric variables, each of which was independently analyzed: mean sea level pressure (MSLP), 500-hPa geopotential heights (500z), 850-hPa temperatures (850t), and the daily mean zonal (U) and meridional (V) components of the zonal wind at 10 m (UVwind). These variables were obtained from the NARR and used to classify a set of typically occurring circulation patterns across the Great Lakes from 1979 to 2015. The spatial extent of each variable was centered over the Great Lakes, with the large-scale circulation variables, 500z and MSLP, having a much larger spatial extent than 850t and UVwind. Prior to classification, a daily spatial gradient was calculated by subtracting the mean of the daily MSLP and 500z field from each grid point's raw value to emphasize the daily pressure and height gradient and to reduce the seasonality of 500z.

Similar to the statistical regionalization, clustering dimensions ranging from 4 clusters to 81 clusters, were assessed using SOMs, k-means, and two-step clustering, with the same cluster validation metrics [the Calinski–Harabasz criterion, the Davies–Bouldin criterion, the silhouette criterion, the variability skill score (Lee 2014), and the distributed variability skill score (Lee 2017)] used to determine the best clustering

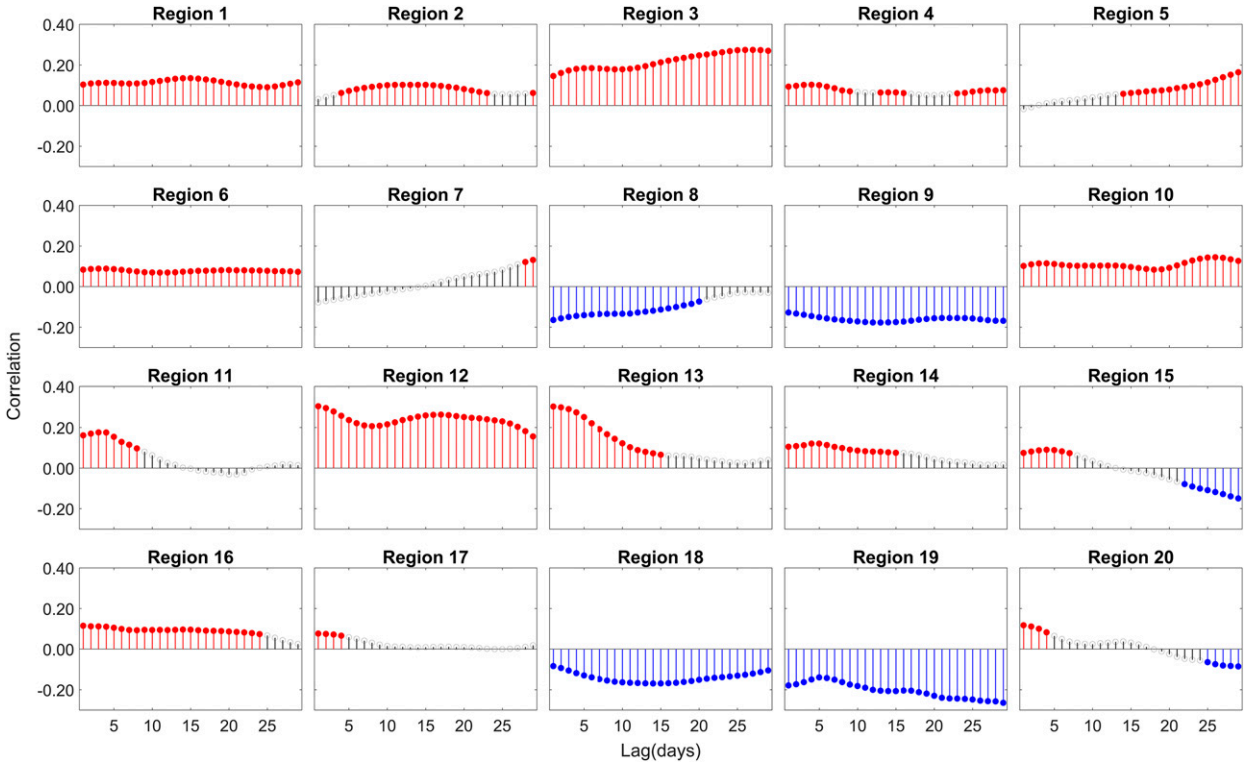

FIG. 5. Correlation between discharge and KDI for each region during spring. Significant correlations ($\alpha \leq 0.05$) are denoted with color-filled points.

solution for the four atmospheric variables. Because the SOM is easier to interpret visually, preference was given to the SOM for clustering solutions that performed similarly across all three clustering methods. Ultimately, the 7 by 5 SOM clustering solution had the best validation scores for 500z, while the 6 by 3 SOM was best for 850t, the 4 by 4 SOM for UVwind, and the 6 by 5 SOM for MSLP. The SOM training process is outlined below.

Each of the four atmospheric variables was first subjected to an s-mode principal components analysis to reduce spatial collinearity (Sheridan and Lee 2011); all principal components (PCs) with eigenvalues greater than 1 were retained for classification. The number of retained PCs and the explained variance of the retained PCs is shown in Table 1. As is noted by Philipp et al. (2014), the artificial neural-network-based SOM method often yields the most stable and reproducible results, which was also found herein for the four atmospheric variables (500z, MSLP, 850t, and UVwind). Furthermore, the SOM method promotes a more intuitive visualization of the classification by organizing the resultant patterns onto a two-dimensional plane with the most different circulation patterns in opposite corners and the most similar ones more nearby (Hewitson and Crane 2002). The SOM "training" began by placing k nodes into random initial starting points within the multidimensional data space, with each node representing one of the final circulation patterns. As the SOM was trained on a batch of observations (e.g., daily fields of MSLP), the algorithm iteratively adjusted the positions of the nodes in the data space to envelop the data cloud, naturally placing more nodes into denser areas of the data-space as it assigned each data point to the node to which it was nearest. In addition to adjusting the position of these "assigned nodes" toward the mean of their member observations, with each pass of the batched data, the position of the nodes that were within a certain radius (using a neighborhood radius parameter defined by the user) of the assigned node in the data space were also adjusted at each step to a lesser degree (using a learning rate parameter, also defined by the user), differentiating the SOM method from other classification techniques, such as k-means (Sheridan and Lee 2011). A SOM array was generated for each of the four variables, and each day in the period of study was assigned to the node in the array it most closely resembled, generating a "calendar" of atmospheric patterns.

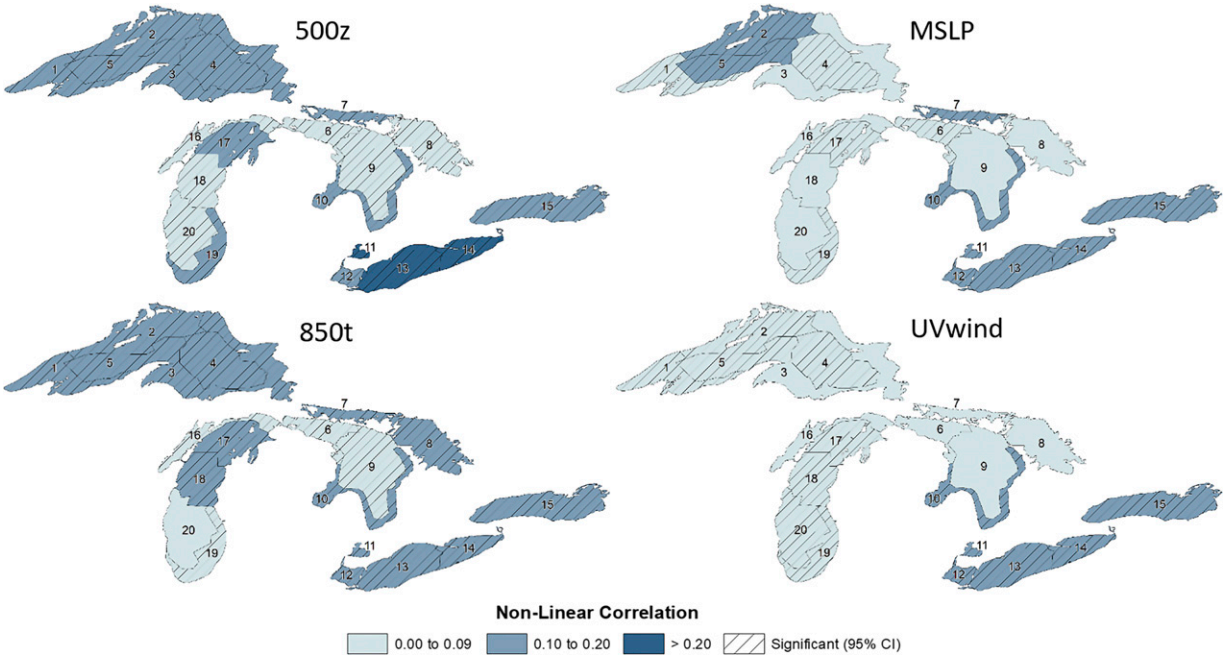

FIG. 6. Nonlinear (eta) correlation between each SOM and KDI by region. Significance at the 95% confidence level is denoted with hatching.

c. *Assessing the relationship between KDI and atmospheric/hydrological variables*

To assess the holistic effect of each SOM (i.e., effect size of the whole SOM, rather than examining each individual pattern within a SOM) on partitioning KDI across CPs, nonlinear (eta) correlations were examined. Based on ANOVA, the eta correlation η measures the nonlinear relationship between a categorical variable (CPs) on a continuous variable (KDI) and is equal to the square root of the sum of squares between the groups/categories/CPs, divided by the total sum of squares:

$$\eta = \sqrt{\frac{\sum_{i=1}^{m}\sum_{j=1}^{n_i}(\overline{X_{i.}} - \overline{X}_{..})^2}{\sum_{i=1}^{m}\sum_{j=1}^{n_i}(X_{ij} - \overline{X}_{..})^2}},$$

where $\overline{X_{i.}}$ denotes the mean KDI of the data for CP i, $\overline{X}_{..}$ is the grand mean of all the KDI data, and X_{ij} denotes the jth observation in the ith CP. More simply, the numerator is calculating the sum of squares between groups/CPs (i.e., the sum of the squared differences between the CP mean KDI and the grand mean KDI), while the denominator is calculating the total sum of squares (i.e., the sum of the squared differences between each data point and the grand mean KDI).

Eta can therefore range between 0 and 1, with larger values indicating a greater effect size (stronger ± nonlinear correlation). The eta correlations were examined for each SOM (500z, 850t, UVwind, and MSLP). To better understand the lagged relationship between KDI and the surface and atmospheric variables, Spearman cross correlations ρ with lags up to 28 days were examined for the linearly detrended daily mean KDI data. The correlations were calculated by region and season to characterize the spatial and temporal fluctuations. The mean daily precipitation for each region's watershed was used to correlate KDI with precipitation. Discharge from individual gauging stations was correlated with KDI, while individual SOM patterns were correlated with KDI for the atmospheric variables. Generalized linear regression was used to assess the relationship between stream discharge volume and KDI.

Because of the large number of variables and regions examined, much of the discussion below focuses on the relationship between KDI and discharge and precipitation for all regions during spring, then narrows the focus to a single region (region 12) and season when discussing the relationship between individual CPs and KDI. Individual CPs will be denoted according to the SOM variable and the pattern number, with the first CP of the 500z, MSLP, 850t, and UVwind SOMs denoted as Z1, S1, T1, and W1, respectively. Lake Erie (regions 12, 13, and 14) was selected because of the water clarity issues impacting the western portion of the lake (region

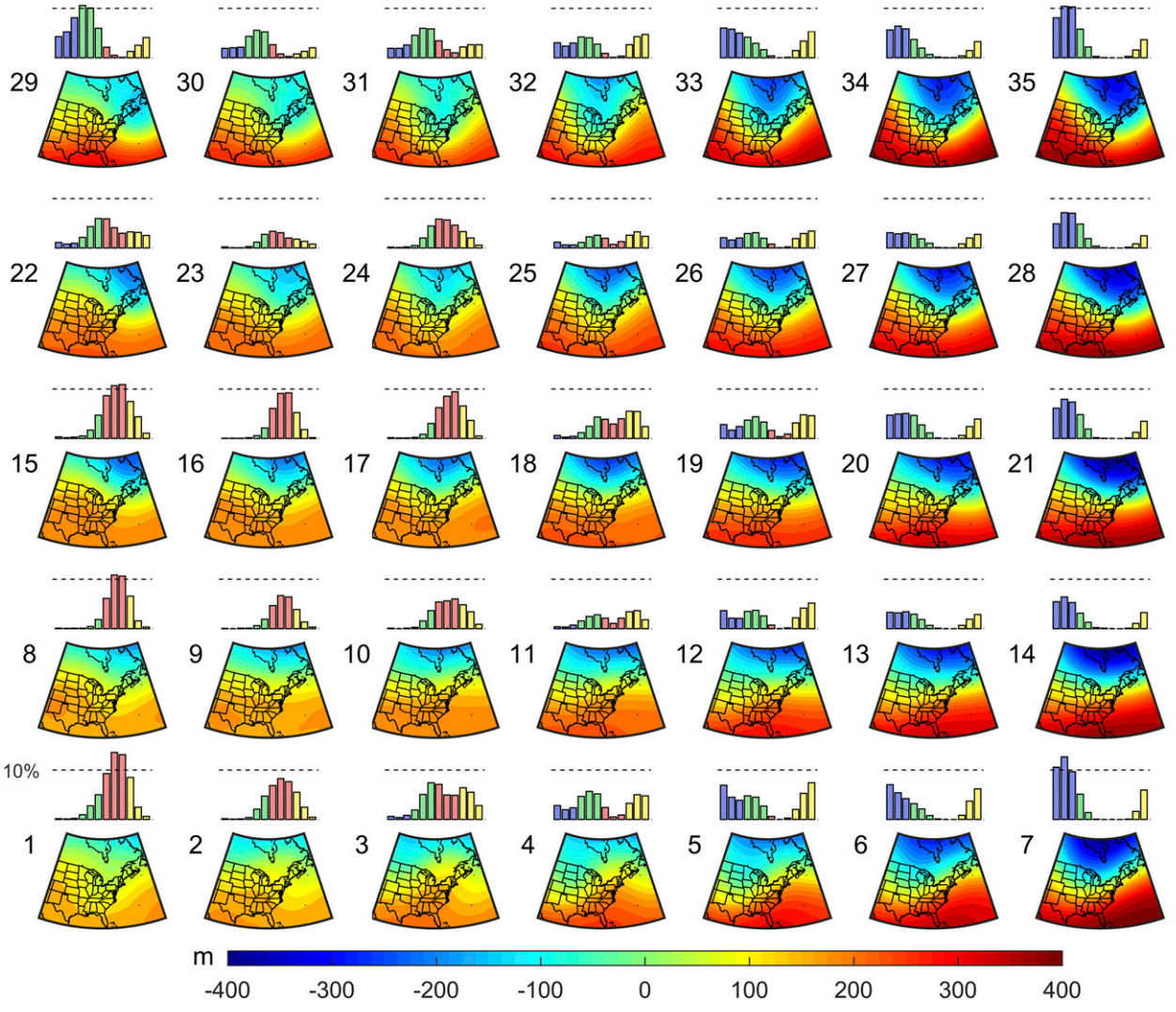

FIG. 7. SOM of the spatial gradient of 500-hPa geopotential height (m) and the seasonality of each pattern (bar graphs). Pattern numbers are placed above the respective SOM patterns. For the bar graph, the months are color coded by season, with blue bars representing the frequency of the SOM pattern occurrence during the three meteorological winter months (December–February), green representing meteorological spring (March–May), red representing meteorological summer (June–August), and yellow representing meteorological autumn (September–November). The dotted line indicates 10% monthly frequency.

12). In this region, the decrease in water clarity is associated with algal blooms that contain toxic cyanobacteria, posing a risk to human life (Michalak et al. 2013). It is also home to the largest human population of the five Great Lakes (Great Lakes Environmental Research Laboratory 2019). Spring was selected because it is a period of large atmospheric variability in the Great Lakes and the time of year when water clarity begins to decline in Lake Erie. Winter was omitted from the discussion because of the large percentage of days with no KDI data due to ice cover and high cloudiness. This is supported by Ackerman et al. (2013) who showed cloud cover for five Great Lakes exceeded 80% during meteorological winter. Furthermore, Mason et al. (2016) showed the 1973–2013 mean duration of ice coverage in Lakes Erie, Huron, and Superior was one to three months, with similar durations in the shallow, near-land portions of Lakes Michigan and Ontario.

3. Results and discussion

a. Trends and variability in KDI

For many regions, the secular trend in KDI accounted for the largest variability in water clarity over the 18-yr period of observation (Fig. 2). With the exception of

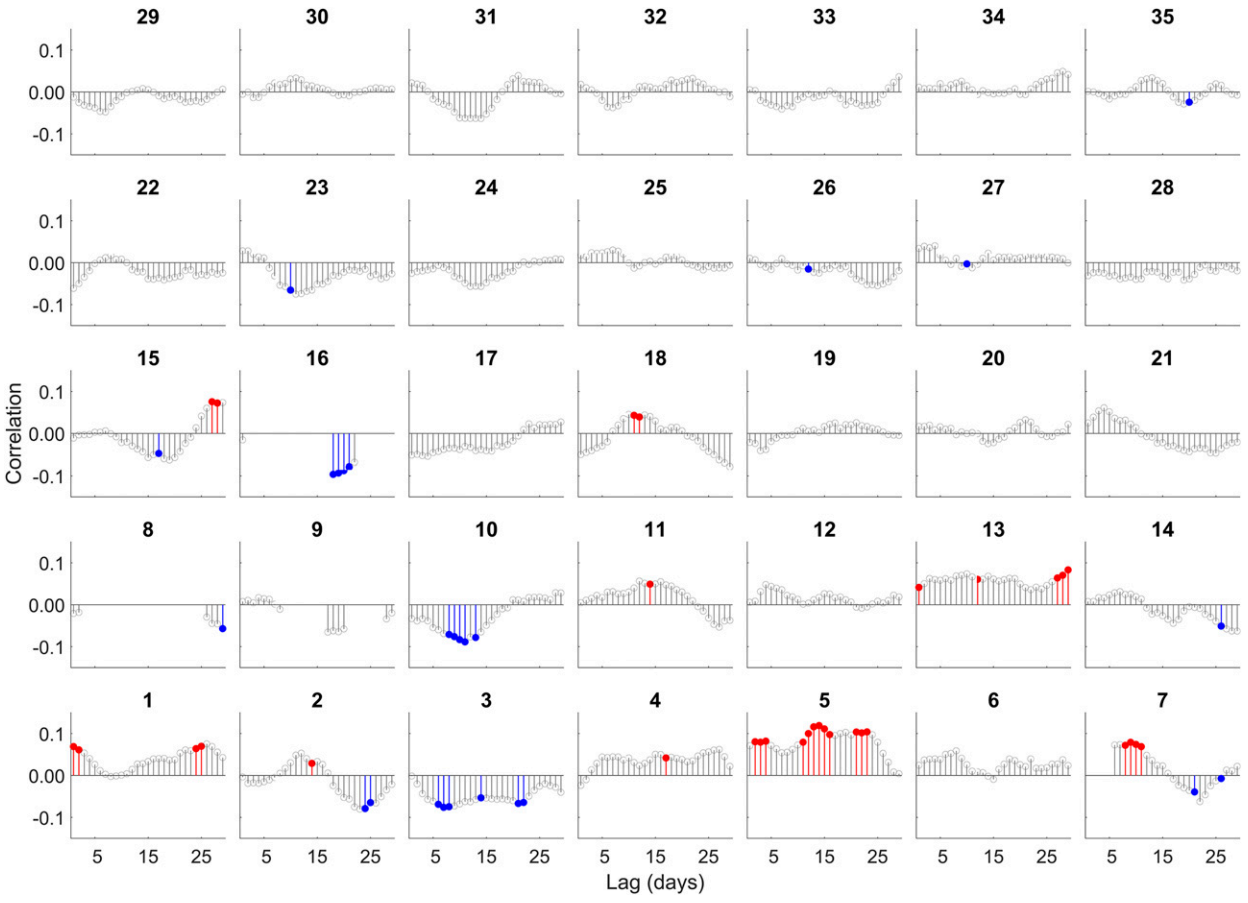

FIG. 8. Correlation of 500z spatial gradient SOM patterns with KDI for region 12 during spring (March–May). Pattern numbers are placed above the respective SOM patterns. Correlations are missing for several summer-dominant patterns for which too few patterns occurred during the spring. Significant correlations ($\alpha \leq 0.05$) are denoted with color-filled points.

regions 13 and 14 in Lake Erie, most of the trends in KDI were negative (i.e., decreased KDI values or increased water clarity). Consistent with the findings from Yousef et al. (2017), the largest negative trends were observed in regions of Lakes Michigan and Huron. This suggests that a major environmental element is resulting in the increased water clarity across regions in Lakes Michigan and Huron, namely, the increase in invasive mussels (Yousef et al. 2017). However, the mussels have also increased rapidly in Lakes Erie and Ontario, which have experienced almost no increase in water clarity and even a slight decrease in clarity (i.e., slight increase in KDI) in regions 13 and 14 in Lake Erie. While the number and species of mussel, along with the rate of increase of the mussels can impact the secular trend, the large discrepancies between lakes suggests another environmental element may be acting to reduce water clarity in these regions. In Lake Erie this may be explained by the reeutrophication since the 1990s that has led to increased algae growth and decreased water clarity (Chapra and Dolan 2012; Robertson and Saad 2011; Scavia et al. 2014).

The monthly mean KDI values for each region (Fig. 3) reveal why the KDI trend in Lakes Michigan and Huron is negative. From late 1997 through 2004, the KDI values in Lakes Michigan and Huron were the highest of the 19-yr period for any lake. The KDI has remained stable in Lakes Erie (regions 12, 13, and 14), Superior (regions 1–5), and Ontario (region 15) throughout much of the time series. This is further supported by the consistency in extreme KDI events [defined by the 20th (clear) and 80th (turbid) percentiles of each region's KDI distribution] in Lakes Erie, Ontario, and Superior (Fig. 4), while Lakes Michigan and Huron, particularly regions 9 and 20, have transitioned from almost no clear events early in the study period to upward of 100 such events per year.

b. Stream discharge and KDI

Stream discharge was the most strongly correlated surface variable with KDI. Smaller streams (by discharge

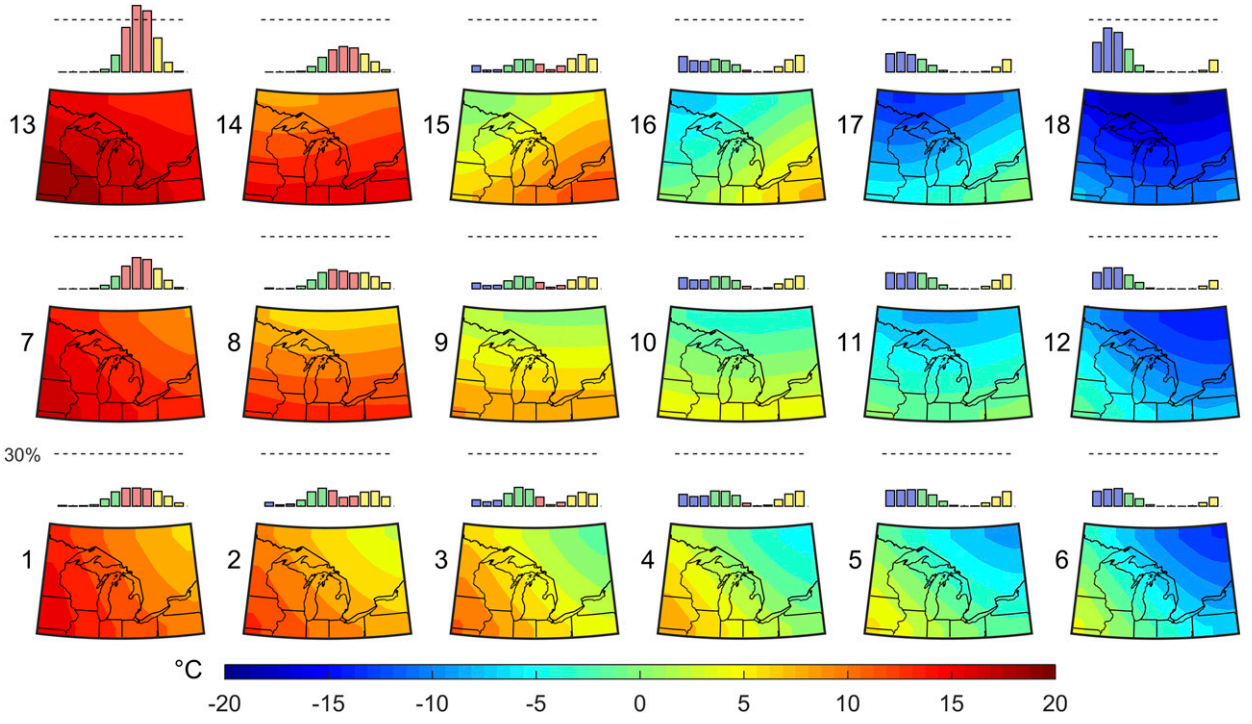

FIG. 9. As in Fig. 7, but for 850t (°C) and the dotted line indicates 30% monthly frequency.

volume) generally had shorter lag periods than larger streams; however, there is no significant relationship between stream size (e.g., average discharge volume) and KDI. For this reason, only the stream with the highest correlation is shown in Fig. 5. The strongest correlations (max $\rho = 0.36$) occurred within a lag of two weeks and were located in the western side of Lake Erie (regions 12 and 13) where algal blooms are most

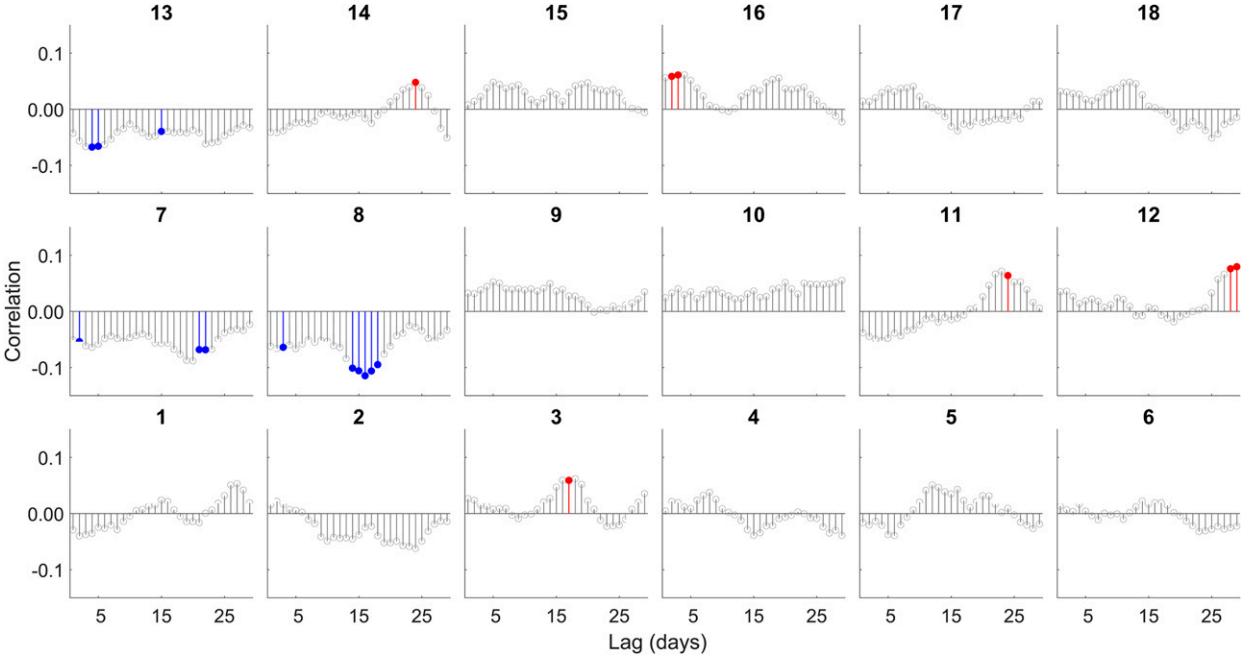

FIG. 10. As in Fig. 8, but for 850t.

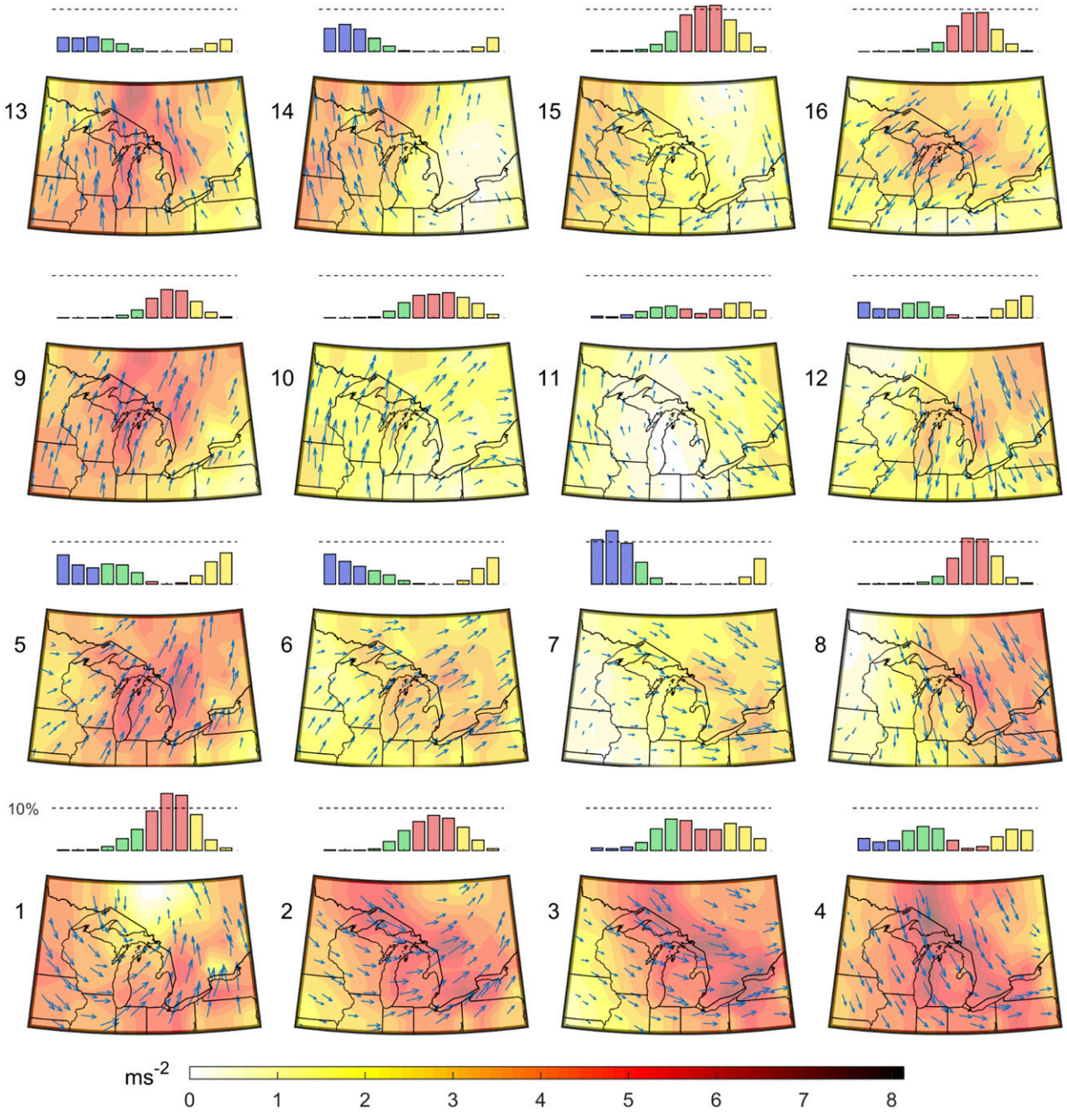

FIG. 11. As in Fig. 7, but for UVwind (shading represents wind magnitude ($m\,s^{-1}$), and the vectors represent wind direction).

prominent and water clarity is typically the lowest (Michalak et al. 2013). Region 3 stream discharge was also highly correlated with KDI; however, the long and narrow shape of the region may influence the time it takes for portions of the region to be affected by stream discharge, resulting in a lag in the larger correlations between KDI and stream discharge. Lakes Michigan (regions 8 and 9) and Huron (regions 18 and 19) had several regions with a negative correlation between stream discharge and KDI during the spring, suggesting increased water clarity following high discharge events. The KDI in the same regions have stronger positive correlations with stream discharge during the summer. The negative correlations (clearer water during higher flow or cloudier water during lower flow) may be a result of frozen ground and a larger areal snowpack during the winter and early spring months, reducing the amount of sediment transport into the lakes via stream

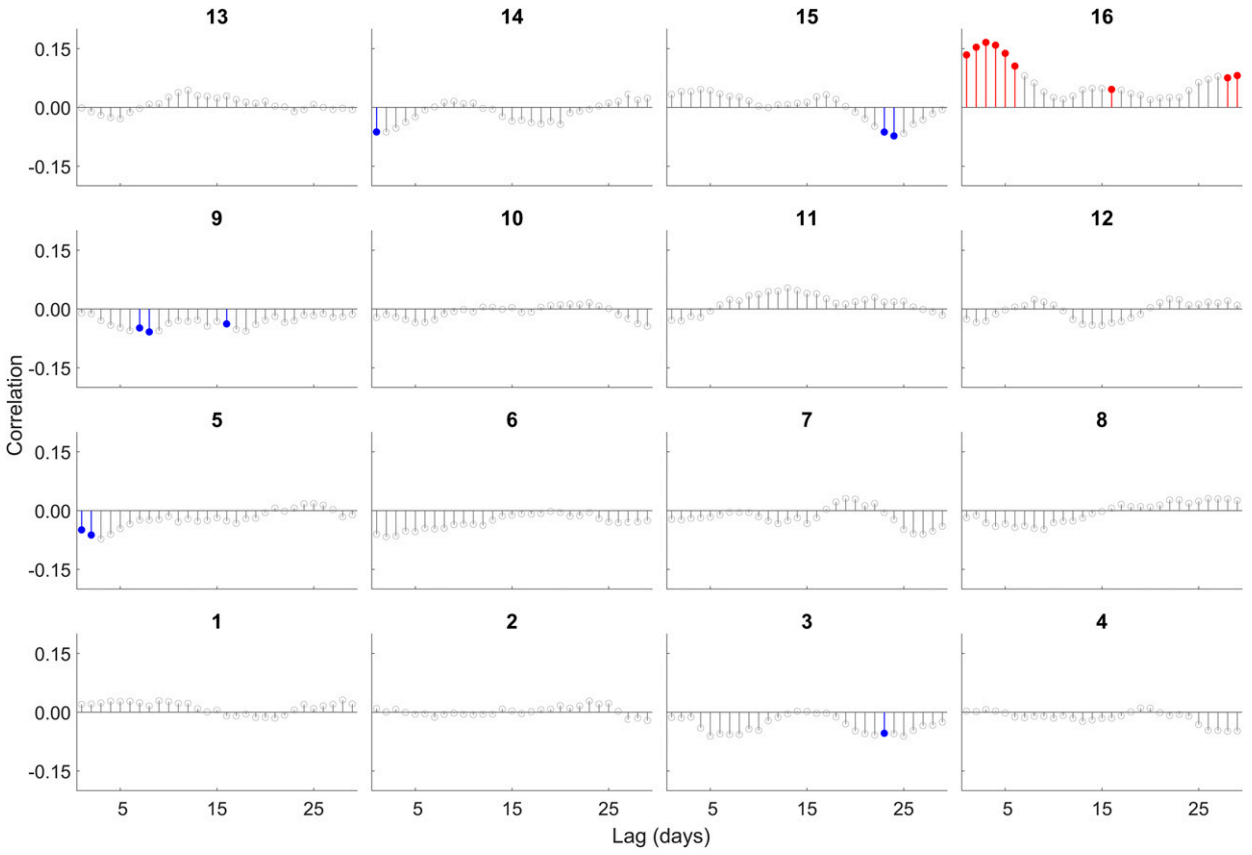

FIG. 12. As in Fig. 8, but for UVwind.

discharge and diluting the present lake water with meltwater. Positive correlations between discharge and KDI may be attributed to snowmelt across an unfrozen surface, increasing the sediment transport into the lakes. These positive correlations may also be attributed to an increase in phosphorus and nitrogen loading from precipitation events during the growing season, supporting the growth of algal blooms during late spring and summer. This is shown by Evans et al. (2018), who found effective soil permeability decreases rapidly below 0°C, and Correll et al. (1999), who found that the nitrogen and phosphorus concentration in the Rhode River watershed in Maryland was much higher during spring and summer than during winter. Furthermore, Michalak et al. (2013) found summer algal blooms in Lake Erie were closely related to increased eutrophication from heavy spring precipitation events.

The correlations between precipitation and KDI were much lower in magnitude with respect to the discharge–KDI correlations. Precipitation, when examined at the mesoscale (summed input of the reanalysis-based precipitation from individual grid points over each region), was poorly correlated with KDI. While more highly correlated, precipitation on a watershed scale is still unable to account for localized conditions such as existing stream levels or the location of precipitation. Mesoscale precipitation events over heavily agricultural areas are likely to contribute more sediment load, phosphorus and nitrogen to the lakes than precipitation events over forested areas. For this reason, the correlations between precipitation and KDI were generally nonsignificant and much lower in magnitude with respect to the discharge–KDI correlations.

c. *SOM patterns and water clarity, with a focus on Lake Erie*

A nonlinear correlation between the four atmospheric SOMs and each KDI region was used to determine the cumulative effect of each SOM on KDI (Fig. 6). The 500z SOM (Fig. 7) generally had the highest correlations with KDI, particularly for regions 13 and 14 in Lake Erie, followed by the 850t, UVwind, and MSLP SOMs (described in more detail below). This relationship is also exhibited between

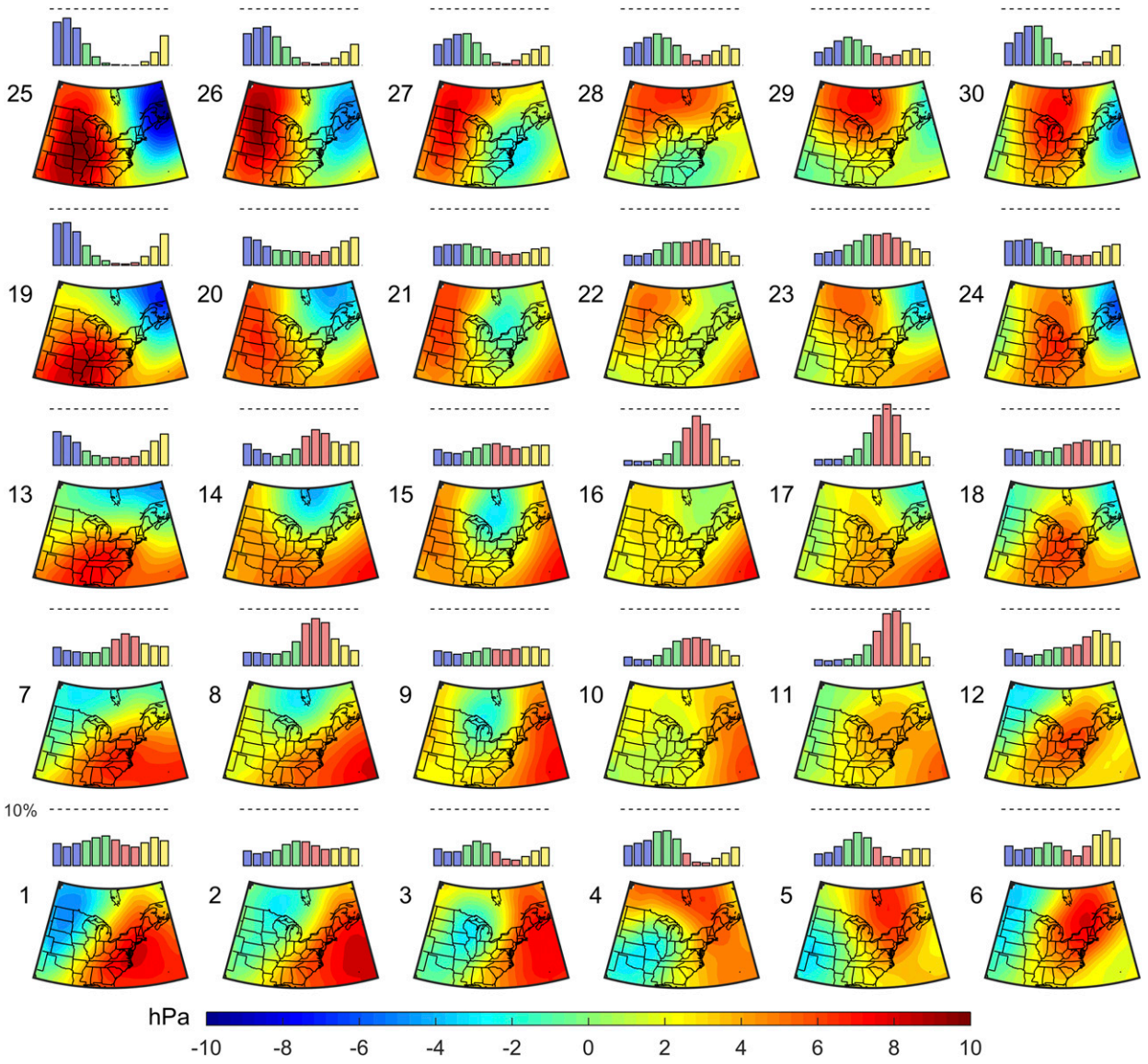

FIG. 13. As in Fig. 7, but for MSLP (hPa).

500z SOM and discharge. Overall, the four different SOMs account for between 11% and 16% of total variability explained in the three Lake Erie regions, with Lake Saint Clair (region 11) being the only other region showing a greater percentage of explained variability in KDI (21%). Lakes Erie and Ontario were consistently higher correlated with the four SOMs than the other lakes. This may be related to the water volume or water circulation patterns in the smaller lakes (Lakes Erie and Ontario) versus the larger lakes (Beletsky et al. 1999), where regions with larger volumes of water are less impacted by circulation patterns than regions with smaller volumes of water (Foley et al. 2012; Kirillin 2010). Regions 9 (Lake Huron) and 20 (Lake Michigan), which experienced the largest changes in KDI during the study period, had the lowest correlations with the four SOMs. The low correlations for much of Lakes Michigan and Huron suggests the water clarity in these regions is likely more dependent on the increased mussel population (and other nonclimate factors) than atmospheric circulation patterns.

The correlation between individual CPs and KDI is seasonally and regionally dependent. For the 500z SOM (Fig. 7), summer-dominant CPs (left side of the SOM) tend to relate to increased water clarity (lower KDI values) in region 12 (Fig. 8). These CPs have lower spatial gradients, favoring drier weather as a result of a more zonal atmospheric flow and less

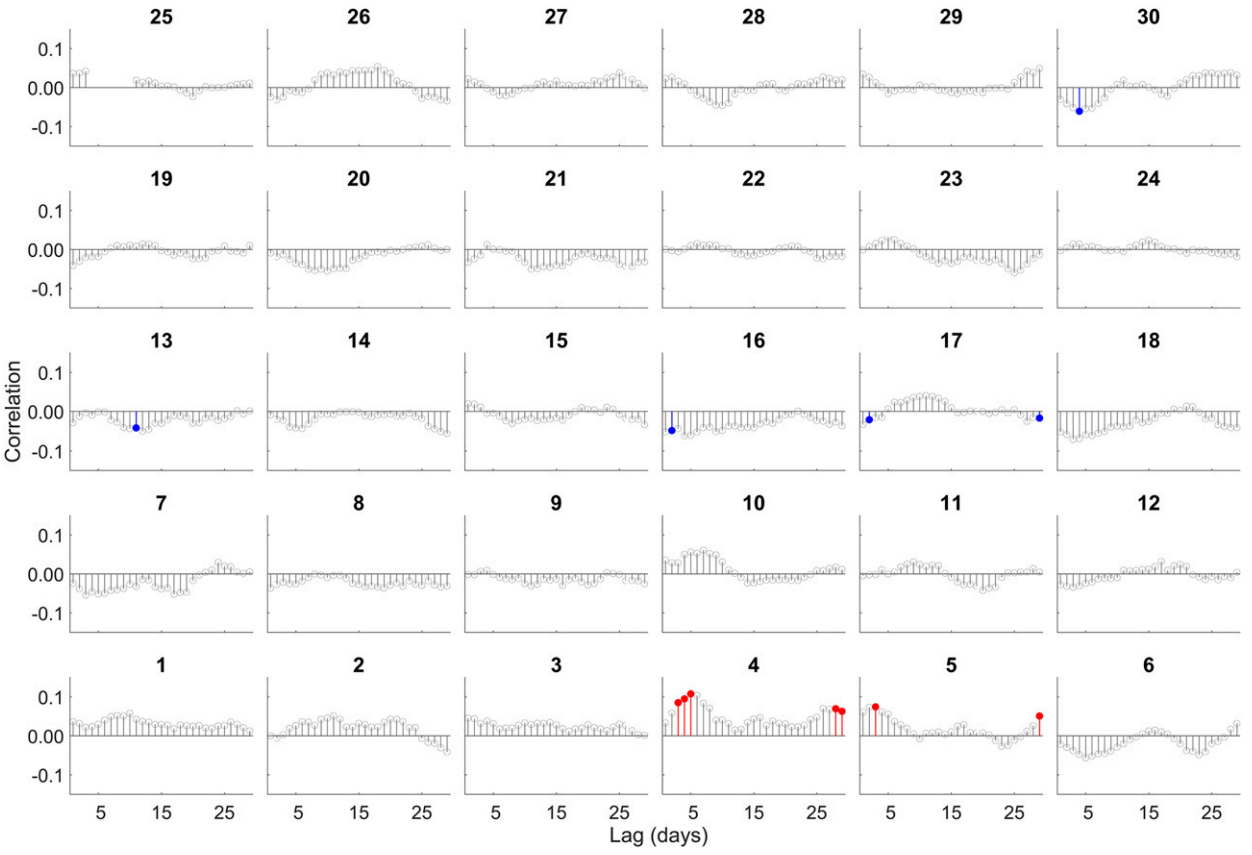

FIG. 14. As in Fig. 8, but for MSLP.

synoptic precipitation events. Transitional CPs, or the less extreme SOM patterns that occur frequently during the transition from fall to winter and spring to summer, tend to favor decreased water clarity. *Z*5—which depicts the Great Lakes just east of an upper-level trough and in an area favorable for cyclogenesis—has the highest and most significant positive correlations (max $\rho = 0.16$) with KDI for region 12, with significant correlations extending three weeks after the CP's occurrence.

The 850t SOM (Fig. 9) has a strong seasonal component, with summer-dominant CPs on the left side of the SOM, winter-dominant CPs on the right side, and transitional CPs in the middle of the SOM (Fig. 10). The summer-dominant CPs, particularly *T*7 and *T*8, exhibit negative correlations (indicating clearer water with increased frequency of these CPs) while the transitional-season CPs show positive correlations for region 12 during spring. This is somewhat counterintuitive, since warmer temperatures stimulate aquatic plant growth, which decreases water clarity (Carr et al. 1997). However, warmer CPs during spring do not necessarily translate to warm water temperatures as the heat capacity of water results in a lag in the warming of the lake. Increased water clarity may therefore be indirectly related to warm CPs through the precipitation patterns associated with each CP during spring.

The UVwind SOM has a lower seasonal component than the 500z and 850t SOMs since winds are more dependent on surface pressure patterns than seasonal temperature fluctuations (Fig. 11). For this reason, the CPs in the UVwind SOM do not tend to cluster by seasonality as CPs in the other SOMs do. While the correlations are primarily nonsignificant, *W*16 is significantly correlated (max $\rho = 0.19$) with KDI in region 12 during spring (Fig. 12). This CP occurs mostly in summer but does (rarely) occur in late spring, bringing light to moderate northeasterly winds in connection with cyclonic circulation around a center of low pressure just to the south of the map. Such winds would likely push any algal blooms in region 13 westward into region 12, thus decreasing water clarity in this region.

Similar to the UVwind SOM, the MSLP SOM has a weaker seasonal component than the 500z and 850t SOMs (Fig. 13). Summer-dominant CPs are generally

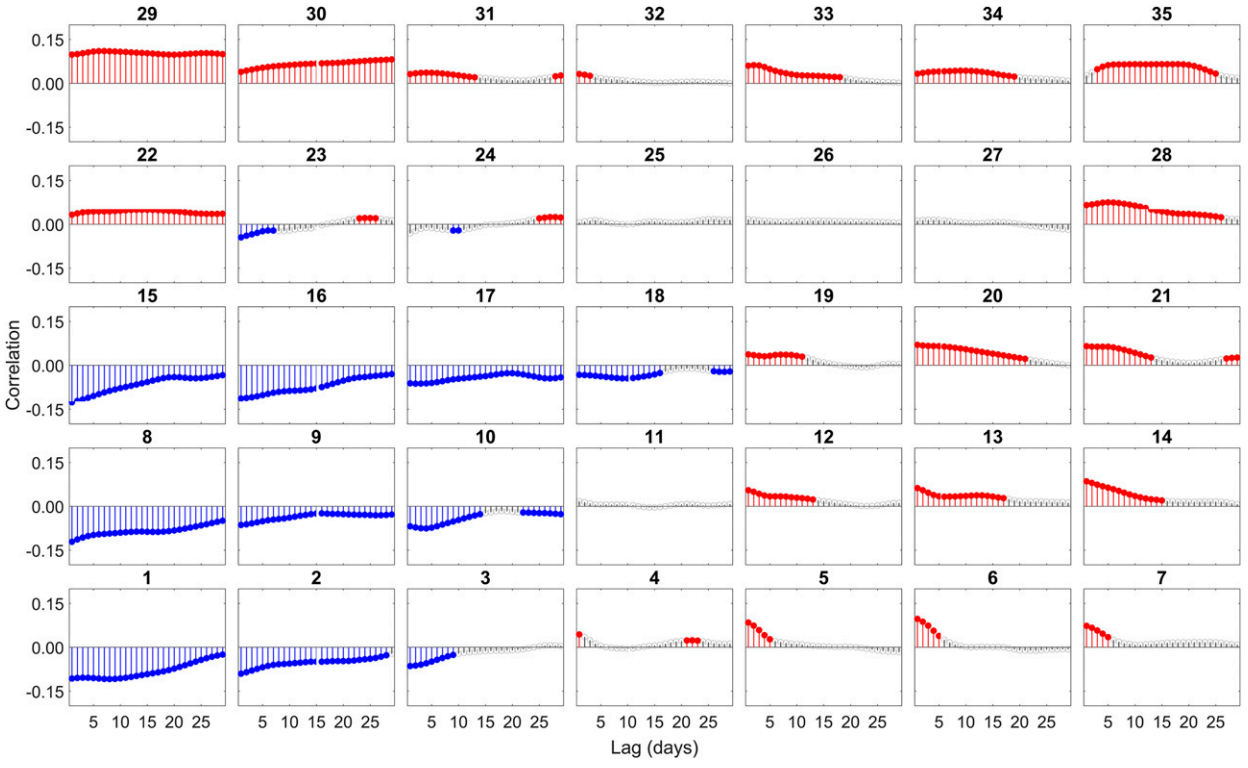

FIG. 15. Correlation of 500z spatial gradient SOM patterns with discharge for region 12 during spring (March–May). Pattern numbers are placed above the respective SOM patterns. Significant correlations ($\alpha \leq 0.05$) are denoted with solid points.

clustered in the right center of the SOM, whereas winter-dominant CPs are clustered in the upper-left side of the SOM. Winter-dominant CPs are the most extreme MSLP CPs with the largest spatial gradients due to an increase in midlatitude cyclones. There is generally no relationship between MSLP CPs and KDI in region 12 during spring as only two CPs (S4 and S30) had significant correlations during the 28-day lag period (Fig. 14). In general, CPs along the lowest row of the SOM showed the greatest positive correlations—each of which depict the Great Lakes between a high pressure to the east and low pressure to the west. S4 exhibits the most significant correlations (max $\rho = 0.15$) within the first 5 days of lag, suggesting a short-term decrease in water clarity in region 12 following S4. Region 12 would likely be on the northeastern fringe of a low pressure system during S4, indicating precipitation and increased stream discharge in the near term. S30 favors decreased water clarity in region 12 during spring. This CP consists of a continental high pressure system centered over the Great Lakes, favoring colder temperatures and less precipitation across region 12.

d. Relationship between SOM patterns and discharge

Whereas the relationship between the CPs and KDI was generally weak and nonsignificant, the relationship between the CPs and discharge was stronger and more significant, particularly with the 500z and 850t CPs. The lagged correlations between 500z and stream discharge (Fig. 15) and 850t and stream discharge (Fig. 16) show that warmer CPs during the spring favor decreased precipitation in region 12, while cooler CPs favor increased precipitation. As shown in Fig. 5, stream discharge is positively correlated with KDI in region 12 during the spring, suggesting that a wet spring leads to decreased water clarity in region 12. Because long-range forecasts of stream discharge are not available, the frequency of 850t and 500z CPs derived from climate models may be used to model subseasonal to seasonal water turbidity in the Great Lakes.

e. Limitations

Since the KDI is satellite derived, cloud cover and ice cover reduce the total number of days with available KDI data. While there are few missing KDI values during meteorological summer and meteorological fall, many of the regions are predominantly ice covered during meteorological winter. For this reason, winter was omitted from the study. Several regions also maintain ice cover through the start of meteorological spring, especially following cold winters, resulting

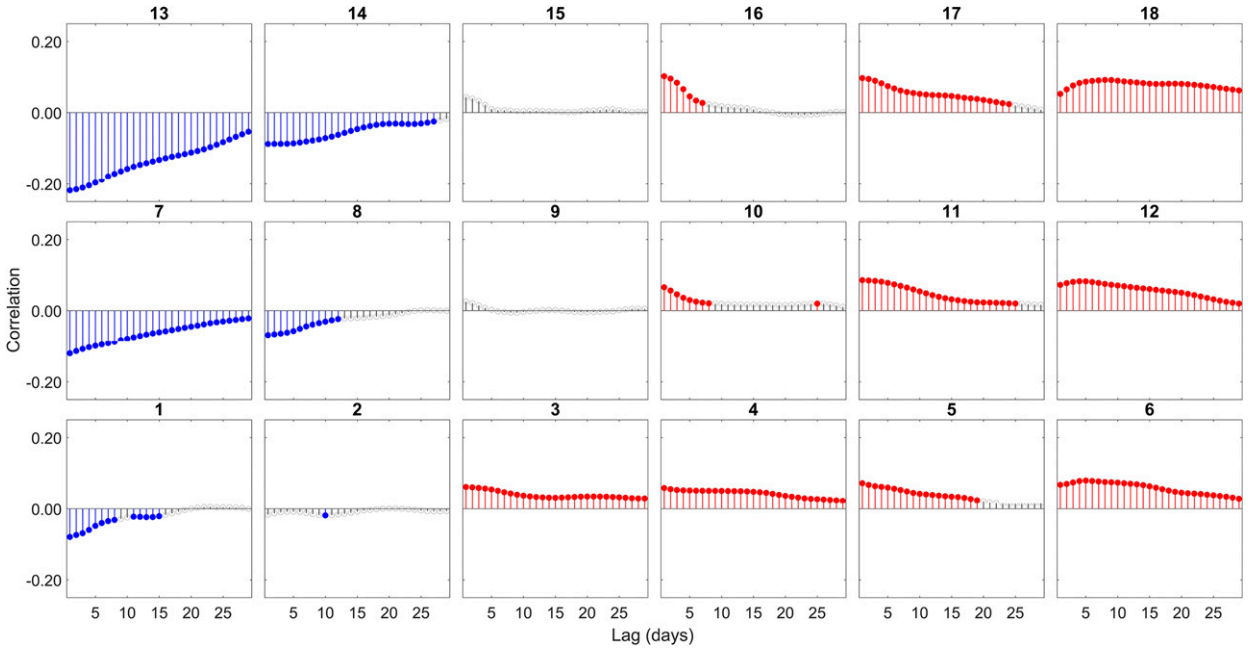

FIG. 16. As in Fig. 15, but for 850t.

in fewer days with KDI data than in summer and fall. Furthermore, the number of SOM patterns used in the pattern classification of each atmospheric variable ultimately impact the results. While a larger number of SOM patterns may better capture small nuances in the atmospheric circulation, it reduces the sample size of patterns for the circulation to environment analysis, thus pattern classification must

TABLE A1. Gauging stations used for each region, with the mean discharge ($m^3 s^{-1}$) in parentheses. The station with the strongest correlation with KDI in each region, which is used to create Fig. 5, is denoted with boldface font.

Region	Gauging stations
Region 1	4024430 (10.96), 4027500 (7.49), **4036000** (4.45), and 4040000 (36.48)
Region 2	**02AB008** (1.53)
Region 3	02BF001 (22.08), 4040500 (0.55), 4041500 (1.11), 4043050 (0.12), 4045500 (2.47), and **4058200** (0.03)
Region 4	02BF001 (22.08), 4040500 (0.55), 4041500 (1.11), 4043050 (0.12), 4045500 (2.47), **4058200** (0.03), 4040000 (36.48), and 4043050 (1.23)
Region 5	4040000 (36.48) and **4043050** (1.23)
Region 6	**02CD001** (20.03)
Region 7	**02CD001** (20.03)
Region 8	02DB005 (36.73), **02DD010** (191.67), 02EA011 (45.23), 02FA002 (1.18), and 02FB010 (5.19)
Region 9	02FA001 (14.60), 02FC001 (62.35), 02FE009 (6.31), 4142000 (9.50), 4151500 (17.43), 4159492 (9.34), 02DB005 (36.73), **02DD010** (191.77), 02EA011 (45.23), and 02FB010 (5.11)
Region 10	**02FA001** (14.61), 02FC001 (62.35), 02FE009 (6.31), 4142000 (9.49), 4151500 (17.42), and 4159492 (9.27)
Region 11	**4166000** (0.75), 4166100 (0.77), and 4166500 (4.44)
Region 12	**4168000** (2.34), 4176500 (24.05), 4177000 (3.64), 4195500 (11.83), 4198000 (36.73), and 4193500 (168.64)
Region 13	02GC026 (9.26), 4200500 (11.27), **4201500** (10.23), 4207200 (4.14), 4208000 (29.55), and 4213000 (8.64)
Region 14	02GC008 (1.95), 02GC026 (9.26), 03021350 (6.39), 04215000 (4.27), 04215500 (7.28), and **4218518** (3.98)
Region 15	02HC018 (1.02), 02HC024 (4.28), 02HC030 (2.56), 02HD010 (0.82), 02HD012 (3.24), 04231000 (3.59), 04231600 (83.21), 04232050 (0.85), 04249000 (201.54), and **4260500** (131.89)
Region 16	**4056500** (38.91), 4059000 (20.60), and 4069500 (24.51)
Region 17	4127800 (5.24), **4056500** (38.91), 4059000 (20.60), and 4069500 (24.51)
Region 18	**4122500** (22.50)
Region 19	4094000 (2.50), 4102500 (13.72), 4102700 (3.01), **4122100** (0.47), 4122200 (13.24), 5528000 (3.08), 5534500 (0.32), 5535000 (0.19), 5535070 (0.32), 5535500 (0.22), 5536000 (1.10), 5536195 (1.92), and 5536290 (2.59)
Region 20	4087000 (14.34), 4087204 (0.73), 4087240 (4.69), 4087257 (1.10), and **5527800** (0.88)

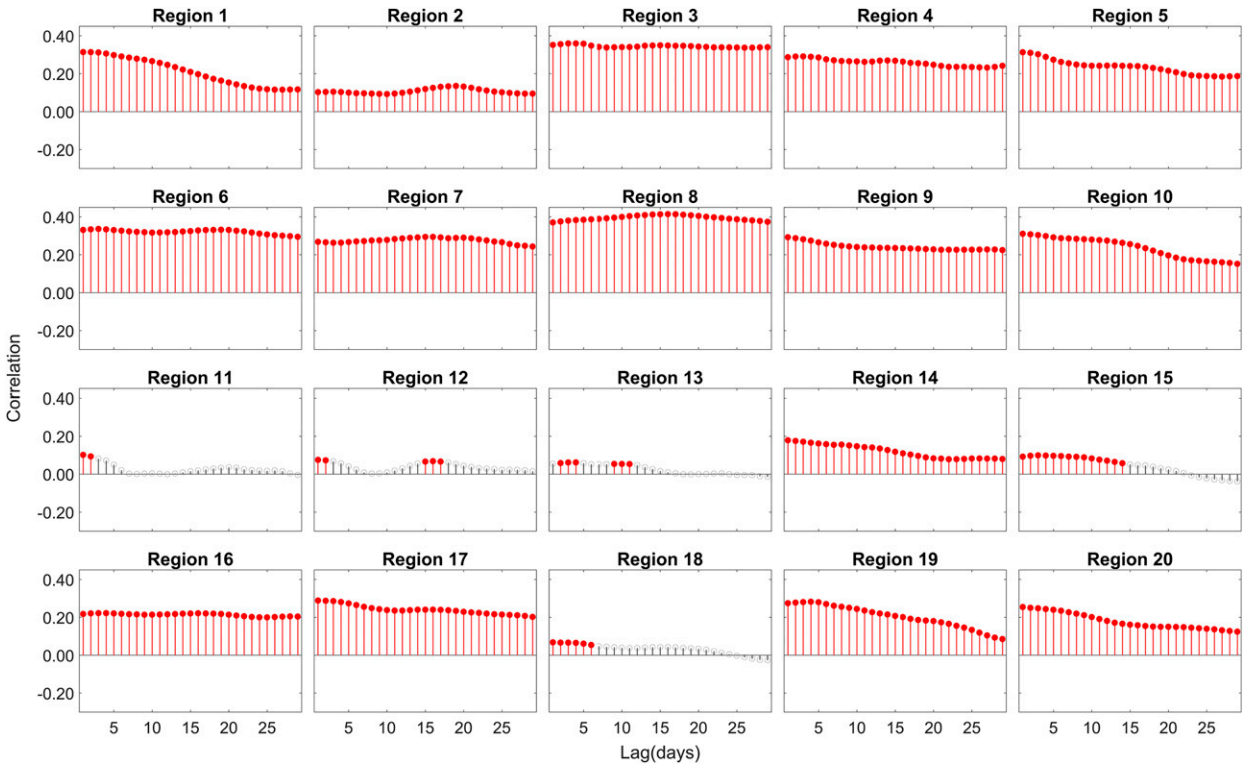

FIG. A1. Correlation between discharge and KDI for each region during summer. Pattern numbers are placed above the respective SOM patterns. Significant correlations ($\alpha \leq 0.05$) are denoted with color-filled points.

strike a balance between too few and too many patterns. This study strives to achieve this balance objectively, although a certain level of subjectivity is always introduced when deciding on the SOM learning parameters and the final SOM dimensions. Last, the impact of hydro control, such as dams, on stream discharge was not assessed.

4. Summary and conclusions

This research utilizes a historical water clarity index (KDI) to investigate the relationship between Great Lakes water clarity and synoptic-scale weather, defined by circulation patterns, and watershed-scale discharge and precipitation. Although the KDI trends in Lakes Superior, Ontario, and Erie are consistent throughout the study period, a negative KDI trend (increased water clarity) in Lakes Michigan and Huron is thought to be related to an increase in invasive mussel species (Yousef et al. 2017). Although invasive mussels are present in other lakes, additional environmental stressors, particularly in Lake Erie, have resulted in periods of increased KDI (decreased water clarity).

Overall, discharge showed the strongest relationship with water clarity, with increasing discharge leading to strong positive correlations in most regions (higher KDI values = cloudier water) and lasting out to 2 or more weeks in many locations—especially in summer. While generally low in magnitude, the nonlinear correlations between each of the four SOMs and KDI reveal that the water clarity in smaller lakes (Lakes Erie and Ontario) tends to be more impacted by circulation patterns than in larger lakes, suggesting water clarity drivers may be dampened by the dynamical processes in lakes with larger surface areas. A closer examination of Lake Erie in spring further suggests the synoptic scale weather does play a small role in impacting day-to-day variably in water clarity. In particular, circulation patterns at various levels that are associated with increased precipitation often show the strongest positive correlations, suggesting sediment and nutrient runoff are the key factors linking the atmosphere to springtime water clarity in the lake. While the magnitude of the correlations between the atmospheric variables and water clarity were generally lower than with discharge, the relationship between the atmospheric CPs and stream discharge was larger and more significant. Because of the significant relationship between atmospheric CPs and stream discharge, long-range forecasts of water clarity in the Great

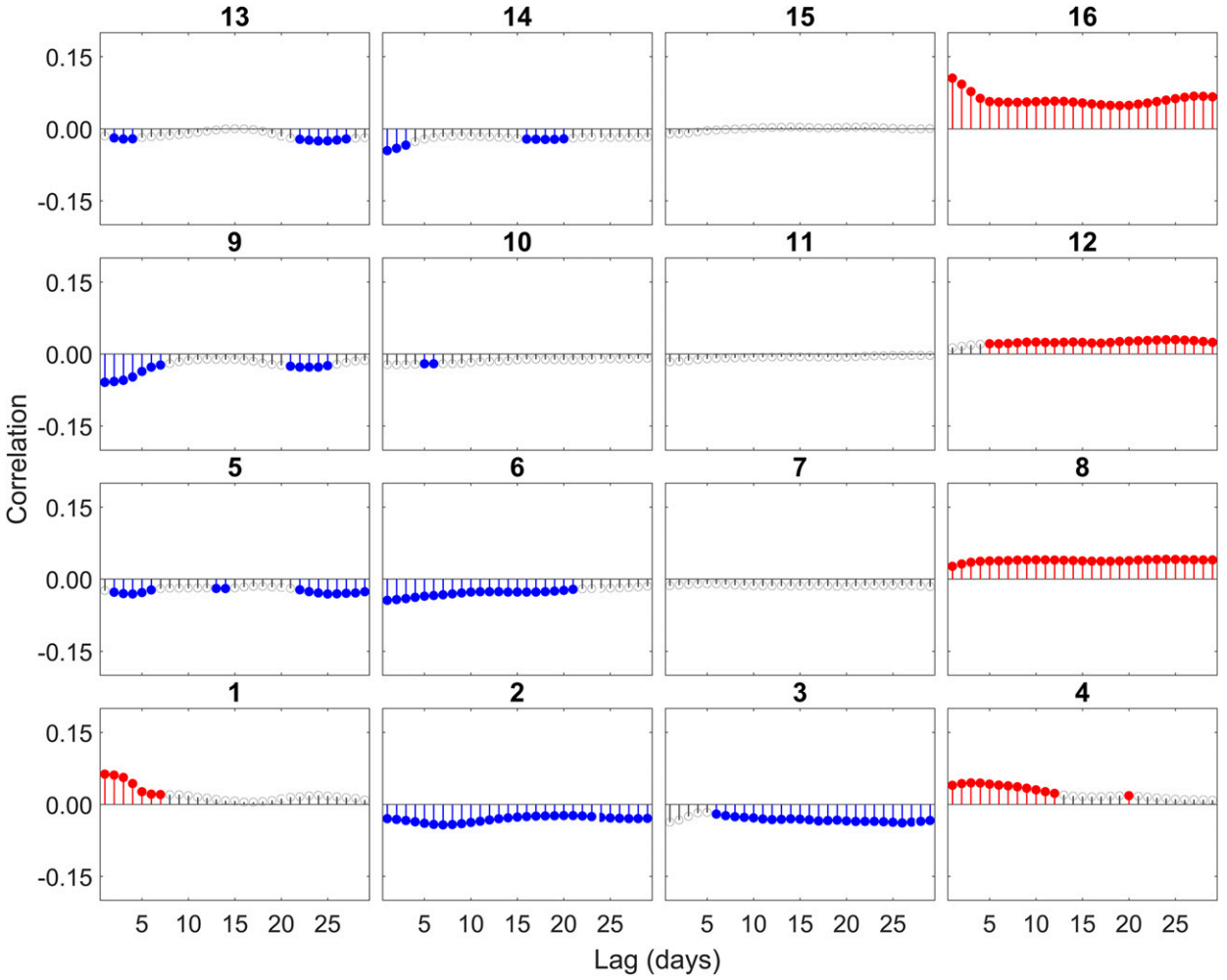

FIG. A2. Correlation between discharge and UVwind for region 12 during spring. Pattern numbers are placed above the respective SOM patterns. Significant correlations ($\alpha \leq 0.05$) are denoted with solid points.

Lakes may benefit by incorporating CPs as a proxy for stream discharge.

The results of this research are currently being used to develop neural-network-based time-series models to empirically predict water clarity in the Great Lakes and generate a complete reconstructed time series of water clarity from 1979 to 2015. Forecast meteorological data will then be combined with the output of the neural-network-based time series models with the goal of producing an operational water clarity outlook for each region in the Great Lakes. The linkage between atmospheric CPs and stream discharge will continue to be explored to improve model input for the operational water clarity outlook. The appendix provides additional figures and tables with details that are relevant to the work presented in this paper.

Acknowledgments. This research was supported by the NASA Research Opportunities in Space and Environmental Sciences (ROSES) funding opportunity, Development and Testing of Potential Indicators for the National Climate Assessment, Award NNX16AH12G. We thank NASA's Ocean Biology Processing Group (OBPG) for providing MODIS data (https://oceancolor.gsfc.nasa.gov), and we thank the reviewers for their comments to improve the presentation of this work.

APPENDIX

Additional Results and Details

Table A1 shows gauging stations used for each region, along with the mean discharge ($m^3 s^{-1}$). It also gives the station with the strongest correlation with KDI in each region (used to create Fig. 5). Figure A1 shows the correlation between discharge and KDI for each region during summer. Figures A2 and A3 show the correlation

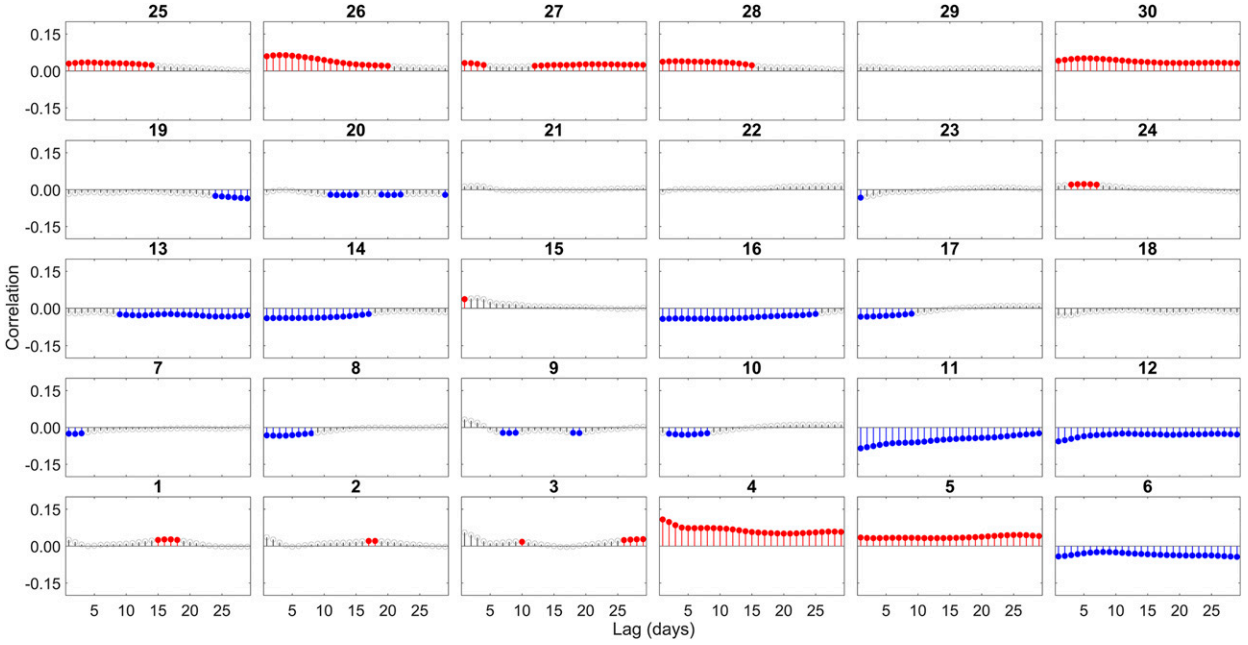

FIG. A3. Correlation between discharge and MSLP for region 12 during spring. Pattern numbers are placed above the respective SOM patterns. Significant correlations ($\alpha \leq 0.05$) are denoted with solid points.

between discharge and UVwind or MSLP, respectively, for region 12 during spring.

REFERENCES

Ackerman, S., A. Heidinger, M. Foster, and B. Maddux, 2013: Satellite regional cloud climatology over the Great Lakes. *Remote Sens.*, **5**, 6223–6240, https://doi.org/10.3390/RS5126223.

Barbiero, R. P., B. M. Lesht, and G. J. Warren, 2011: Evidence for bottom–up control of recent shifts in the pelagic food web of Lake Huron. *J. Great Lakes Res.*, **37**, 78–85, https://doi.org/10.1016/j.jglr.2010.11.013.

Beletsky, D., J. H. Saylor, and D. J. Schwab, 1999: Mean circulation in the Great Lakes. *J. Great Lakes Res.*, **25**, 78–93, https://doi.org/10.1016/S0380-1330(99)70718-5.

Binding, C. E., J. H. Jerome, R. P. Bukata, and W. G. Booty, 2007: Trends in water clarity of the lower Great Lakes from remotely sensed aquatic color. *J. Great Lakes Res.*, **33**, 828–841, https://doi.org/10.3394/0380-1330(2007)33[828:TIWCOT]2.0.CO;2.

Carr, G. M., H. C. Duthie, and W. D. Taylor, 1997: Models of aquatic plant productivity: A review of the factors that influence growth. *Aquat. Bot.*, **59**, 195–215, https://doi.org/10.1016/S0304-3770(97)00071-5.

Chapra, S. C., and D. M. Dolan, 2012: Great Lakes total phosphorus revisited: 2. Mass balance modeling. *J. Great Lakes Res.*, **38**, 741–754, https://doi.org/10.1016/j.jglr.2012.10.002.

Correll, D. L., T. E. Jordan, and D. E. Weller, 1999: Transport of nitrogen and phosphorus from Rhode River watersheds during storm events. *Water Resour. Res.*, **35**, 2513–2521, https://doi.org/10.1029/1999WR900058.

Davies-Colley, R. J., and D. G. Smith, 2001: Turbidity suspended sediment, and water clarity: A review. *J. Amer. Water Resour. Assoc.*, **37**, 1085–1101, https://doi.org/10.1111/j.1752-1688.2001.tb03624.x.

Dobiesz, N. E., and N. P. Lester, 2009: Changes in mid-summer water temperature and clarity across the Great Lakes between 1968 and 2002. *J. Great Lakes Res.*, **35**, 371–384, https://doi.org/10.1016/j.jglr.2009.05.002.

Evans, S. G., S. Ge, C. I. Voss, and N. P. Molotch, 2018: The role of frozen soil in groundwater discharge predictions for warming alpine watersheds. *Water Resour. Res.*, **54**, 1599–1615, https://doi.org/10.1002/2017WR022098.

Fahnenstiel, G., S. Pothoven, H. Vanderploeg, D. Klarer, T. Nalepa, and D. Scavia, 2010: Recent changes in primary production and phytoplankton in the offshore region of southeastern Lake Michigan. *J. Great Lakes Res.*, **36**, 20–29, https://doi.org/10.1016/j.jglr.2010.03.009.

Foley, B., I. D. Jones, S. C. Maberly, and B. Rippey, 2012: Long-term changes in oxygen depletion in a small temperate lake: Effects of climate change and eutrophication. *Freshwater Biol.*, **57**, 278–289, https://doi.org/10.1111/j.1365-2427.2011.02662.x.

Fuller, K., H. Shear, and J. Wittig, Eds., 1995: The Great Lakes: An environmental atlas and resource book. U.S. EPA Tech. Rep. 905-B-95-001, 46 pp.

Great Lakes Environmental Research Laboratory, 2019: About our Great Lakes: Lake by lake profiles. NOAA, accessed 5 May 2019, https://www.glerl.noaa.gov/education/ourlakes/lakes.html.

Hewitson, B., and R. Crane, 2002: Self-organizing maps: Applications to synoptic climatology. *Climate Res.*, **22**, 13–26, https://doi.org/10.3354/cr022013.

Kirillin, G., 2010: Modeling the impact of global warming on water temperature and seasonal mixing regimes in small temperate lakes. *Boreal Environ. Res.*, **15**, 279–293.

Krantzberg, G., and C. D. Boer, 2006: A valuation of ecological services in the Great Lakes Basin ecosystem to sustain healthy communities and a dynamic economy. McMaster University Dofasco Centre for Engineering and Public Policy Rep., 99 pp., http://longpointbiosphere.com/download/Environment/krantz2.pdf.

Lee, C. C., 2014: The development of a gridded weather typing classification scheme. *Int. J. Climatol.*, **35**, 641–659, https://doi.org/10.1002/joc.4010.

——, 2017: Reanalysing the impacts of atmospheric teleconnections on cold-season weather using multivariate surface weather types and self-organizing maps. *Int. J. Climatol.*, **37**, 3714–3730, https://doi.org/10.1002/joc.4950.

——, S. C. Sheridan, B. B. Barnes, C. Hu, D. E. Pirhalla, V. Ransibrahmanakul, and K. Shein, 2017: The development of a non-linear autoregressive model with exogenous input (NARX) to model climate-water clarity relationships: Reconstructing a historical water clarity index for the coastal waters of the southeastern USA. *Theor. Appl. Climatol.*, **130**, 557–569, https://doi.org/10.1007/s00704-016-1906-7.

Lee, Z., K.-P. Du, and R. Arnone, 2005: A model for the diffuse attenuation coefficient of downwelling irradiance. *J. Geophys. Res.*, **110**, C02016, https://doi.org/10.1029/2004JC002275.

——, and Coauthors, 2018: Global water clarity: Continuing a century-long monitoring. *Eos, Trans. Amer. Geophys. Union*, **99**, https://doi.org/10.1029/2018EO097251.

Makarewicz, J. C., T. W. Lewis, and P. Bertram, 1999: Phytoplankton composition and biomass in the offshore waters of Lake Erie: Pre- and post-*Dreissena* introduction (1983–1993). *J. Great Lakes Res.*, **25**, 135–148, https://doi.org/10.1016/S0380-1330(99)70722-7.

Mason, L. A., C. M. Riseng, A. D. Gronewold, E. S. Rutherford, J. Wang, A. Clites, S. D. P. Smith, and P. B. Mcintyre, 2016: Fine-scale spatial variation in ice cover and surface temperature trends across the surface of the Laurentian Great Lakes. *Climatic Change*, **138**, 71–83, https://doi.org/10.1007/s10584-016-1721-2.

Mesinger, F., and Coauthors, 2006: North American Regional Reanalysis. *Bull. Amer. Meteor. Soc.*, **87**, 343–360, https://doi.org/10.1175/BAMS-87-3-343.

Michalak, A. M., and Coauthors, 2013: Record-setting algal bloom in Lake Erie caused by agricultural and meteorological trends consistent with expected future conditions. *Proc. Natl. Acad. Sci. USA*, **110**, 6448–6452, https://doi.org/10.1073/pnas.1216006110.

Millie, D. F., G. L. Fahnenstiel, J. D. Bressie, R. J. Pigg, R. R. Rediske, D. M. Klarer, P. A. Tester, and R. W. Litaker, 2009: Late-summer phytoplankton in western Lake Erie (Laurentian Great Lakes): Bloom distributions, toxicity, and environmental influences. *Aquat. Ecol.*, **43**, 915–934, https://doi.org/10.1007/s10452-009-9238-7.

Nalepa, T. F., D. L. Fanslow, and G. A. Lang, 2009: Transformation of the offshore benthic community in lake Michigan: Recent shift from the native amphipod *Diporeia* spp. to the invasive mussel *Dreissena rostriformis bugensis*. *Freshwater Biol.*, **54**, 466–479, https://doi.org/10.1111/j.1365-2427.2008.02123.x.

——, ——, and S. A. Pothoven, 2010: Recent changes in density, biomass, recruitment, size structure, and nutritional state of *Dreissena* populations in southern Lake Michigan. *J. Great Lakes Res.*, **36**, 5–19, https://doi.org/10.1016/j.jglr.2010.03.013.

Niemistö, J., 2008: Sediment resuspension as a water quality regulator in lakes. Ph.D. dissertation, University of Helsinki, 47 pp.

Philipp, A., C. Beck, S. Kaspar, and J. Jacobeit, 2014: Combining artificial neural networks and circulation type classification: Does it improve downscaling models? *Geophysical Research Abstracts*, Vol. 16, Abstract EGU2014-16395-1, https://meetingorganizer.copernicus.org/EGU2014/EGU2014-16395-1.pdf.

Pirhalla, D. E., S. C. Sheridan, V. Ransibrahmanakul, and C. C. Lee, 2014: Assessing cold-snap and mortality events in South Florida coastal ecosystems: Development of a biological cold stress index using satellite SST and weather pattern forcing. *Estuaries Coasts*, **38**, 2310–2322, https://doi.org/10.1007/s12237-014-9918-y.

Ransibrahmanakul, V., S. J. Pittman, D. E. Pirhalla, S. C. Sheridan, C. C. Lee, B. B. Barnes, C. Hu, and K. Shein, 2018: Linking weather patterns, water quality and invasive mussel distributions in the development and application of a water clarity index for the Great Lakes. *IEEE Int. Geoscience and Remote Sensing Symp.*, Valencia, Spain, IEEE, https://doi/org/10.1109/IGARSS.2018.8518935.

Rennie, M. D., W. G. Sprules, and T. B. Johnson, 2009: Resource switching in fish following a major food web disruption. *Oecologia*, **159**, 789–802, https://doi.org/10.1007/s00442-008-1271-z.

Ricciardi, A., F. G. Whoriskey, and J. B. Rasmussen, 1997: The role of the zebra mussel (*Dreissena polymorpha*) in structuring macroinvertebrate communities on hard substrata. *Can. J. Fish. Aquat. Sci.*, **54**, 2596–2608, https://doi.org/10.1139/f97-174.

Robertson, D. M., and D. A. Saad, 2011: Nutrient inputs to the Laurentian Great Lakes by source and watershed estimated using SPARROW watershed models. *J. Amer. Water Resour. Assoc.*, **47**, 1011–1033, https://doi.org/10.1111/j.1752-1688.2011.00574.x.

Scavia, D., and Coauthors, 2014: Assessing and addressing the re-eutrophication of Lake Erie: Central basin hypoxia. *J. Great Lakes Res.*, **40**, 226–246, https://doi.org/10.1016/J.JGLR.2014.02.004.

Sheridan, S. C., and C. C. Lee, 2011: The self-organizing map in synoptic climatological research. *Prog. Phys. Geogr.*, **35**, 109–119, https://doi.org/10.1177/0309133310397582.

——, D. E. Pirhalla, C. C. Lee, and V. Ransibrahmanakul, 2013: Evaluating linkages of weather patterns and water quality responses in South Florida using a synoptic climatological approach. *J. Appl. Meteor. Climatol.*, **52**, 425–438, https://doi.org/10.1175/JAMC-D-12-0126.1.

——, C. Hu, C. C. Lee, B. Barnes, D. Pirhalla, V. Ransi, and K. A. Shein, 2014: Development of a water clarity index for the southeastern U.S. as a climate indicator. *2014 Fall Meeting*, San Francisco, CA, Amer. Geophys. Union, Abstract GC51B-0407.

Shuchman, R. A., K. R. Bosse, M. J. Sayers, G. L. Fahnenstiel, and G. Leshkevich, 2017: Satellite observed water quality changes in the Laurentian Great lakes due to invasive species, anthropogenic forcing, and climate change. *Int. Arch. Photogramm. Remote Sens. Spat. Inf. Sci*, **XLII-3**, 189–195, https://doi.org/10.5194/isprs-archives-XLII-3-W2-189-2017.

Skubinna, J. P., T. G. Coon, and T. R. Batterson, 1995: Increased abundance and depth of submersed macrophytes in response to decreased turbidity in Saginaw Bay, Lake Huron. *J. Great Lakes Res.*, **21**, 476–488, https://doi.org/10.1016/S0380-1330(95)71060-7.

Thiery, W., A. Martynov, F. Darchambeau, J. P. Descy, P. D. Plisnier, L. Sushama, and N. P. van Lipzig, 2014: Understanding the performance of the Flake model over two African Great Lakes. *Geosci. Model Dev.*, **7**, 317–337, https://doi.org/10.5194/GMD-7-317-2014.

Trumpickas, J., B. J. Shuter, and C. K. Minns, 2009: Forecasting impacts of climate change on Great Lakes surface water temperatures. *J. Great Lakes Res.*, **35**, 454–463, https://doi.org/10.1016/j.jglr.2009.04.005.

U.S. Geological Survey, 2017: USGS water data for the nation. National water information system data: Web interface. U.S. Department of the Interior, accessed 6 February 2017, http://waterdata.usgs.gov/nwis/.

Vanderploeg, H. A., J. R. Liebig, W. W. Carmichael, M. A. Agy, T. H. Johengen, G. L. Fahnenstiel, and T. F. Nalepa, 2001: Zebra mussel (Dreissena polymorpha) selective filtration

promoted toxic microcystis blooms in Saginaw Bay (Lake Huron) and Lake Erie. *Can. J. Fish. Aquat. Sci.*, **58**, 1208–1221, https://doi.org/10.1139/f01-066.

Water Survey of Canada, 2017: HYDAT. Accessed 2 February 2018, https://www.canada.ca/en/environment-climate-change/services/water-overview/quantity/monitoring/survey.html.

Watson, S. B., and Coauthors, 2016: The re-eutrophication of Lake Erie: Harmful algal blooms and hypoxia. *Harmful Algae*, **56**, 44–66, https://doi.org/10.1016/j.hal.2016.04.010.

Yousef, F., R. Shuchman, M. Sayers, G. Fahnenstiel, and A. Henareh, 2017: Water clarity of the Upper Great Lakes: Tracking changes between 1998–2012. *J. Great Lakes Res.*, **43**, 239–247, https://doi.org/10.1016/j.jglr.2016.12.002.

Zhao, J., B. Barnes, N. Melo, D. English, B. Lapointe, F. Muller-Karger, B. Schaeffer, and C. Hu, 2013: Assessment of satellite-derived diffuse attenuation coefficients and euphotic depths in South Florida coastal waters. *Remote Sens. Environ.*, **131**, 38–50, https://doi.org/10.1016/j.rse.2012.12.009.